The role of quench rate on the plastic flow and fracture of three aluminium alloys with different grain structure and texture

Bjørn Håkon Frodal [a,b,*], Emil Christiansen [b,c], Ole Runar Myhr [a,d], Odd Sture Hopperstad [a,b]

[a] Structural Impact Laboratory (SIMLab), Department of Structural Engineering, Norwegian University of Science and Technology (NTNU), Trondheim NO-7491, Norway
[b] Centre for Advanced Structural Analysis (CASA), NTNU, Trondheim NO-7491, Norway
[c] Department of Physics, Norwegian University of Science and Technology (NTNU), Trondheim NO-7491, Norway
[d] Hydro Aluminium, Research and Technology Development (RTD), Sunndalsøra NO-6601, Norway

ARTICLE INFO

ABSTRACT

The yielding, plastic flow and fracture of age hardenable aluminium alloys depend on the quench rate to room temperature after the solution heat-treatment at elevated temperature and before the artificial ageing. We investigate three AlMgSi alloys with different grain structure and crystallographic texture experimentally to determine the effects of quench rate (either water-quenching or air-cooling) on the precipitate microstructure and the mechanical properties, i.e., yield stress, work hardening and ductility. Tensile tests on smooth and V-notch specimens and Kahn tear tests are performed to study the influence of stress state on plastic flow and fracture. In addition, finite element simulations of the mechanical tests are performed for one of the alloys to investigate the validity of an extension of the Gurson model to high-exponent anisotropic plasticity. Transmission electron microscopy investigations show that the alloys and their precipitation microstructure are differently affected by the quench rate. Common for the three alloys is that the precipitate free zones around dispersoids and grain boundaries become larger, and the yield strength of the alloys becomes lower, after air-cooling than after water-quenching. The nanostructure model NaMo was modified to account for precipitate free zones, and was able to predict both the precipitation parameters and the tensile yield strength of all tempers and materials with a reasonable degree of accuracy, except in one case. In this case, the inhomogeneous precipitation in the material is too complex to be captured by the inherent precipitation model in NaMo. Due to the lower yield strength and higher work-hardening rate after air-cooling, the failure strain is increased for the smooth and V-notch tensile tests. The crack propagation energy, calculated from the Kahn tear tests, is markedly affected by the quench rate and the effect is different depending on the grain structure and plastic anisotropy, caused by the crystallographic texture. The anisotropic porous plasticity model used in the finite element simulations is able to precisely capture the fracture initiation in all the specimen geometries of the considered alloy, whereas the crack propagation energies of the Kahn tear tests are slightly overestimated.

* Corresponding author at: Structural Impact Laboratory (SIMLab), Department of Structural Engineering, Norwegian University of Science and Technology (NTNU), NO-7491 Trondheim, Norway.
E-mail address: bjorn.h.frodal@ntnu.no (B.H. Frodal).

1. Introduction

Age hardenable aluminium alloys are widely used, such as in car body panels, aeroplane fuselages, and in load-bearing components for structural applications. High strength and ductility are typically desired for practical applications, and aluminium alloys are attractive due to their high load-bearing capacity and low weight. In addition, properties such as good formability and corrosion resistance, combined with a great potential for recycling, make them appealing to, e.g., the automotive and offshore industry. The thermo-mechanical processing of age hardenable aluminium alloys influences microstructural characteristics such as the grain structure, crystallographic texture and precipitate structure. Thus, by changing the chemical composition, heat treatment and mechanical processing, one can control the yield stress, work hardening and plastic anisotropy of the alloy. While this flexibility is desired, it can also give rise to processing related issues such as quench sensitivity. The quench rate after homogenization or the solution heat-treatment can affect the age hardening capability of these alloys and slower cooling rates can lead to a lower strength (Dons & Lohne, 1983). Albeit high quench rates are favourable to attain preferred mechanical properties, it is not always achievable in practical applications, and in industry it is a common practice to limit the quench rate to prevent distortion (Strobel et al., 2016).

Quench sensitivity is primarily caused by the precipitation of non-strengthening phases on dispersoids and at grain boundaries during cooling, and the number density of the dispersoids is known to increase quench sensitivity (Conserva & Fiorini, 1973; Deschamps, Texier, Ringeval, & Delfaut-Durut, 2009; Dons & Lohne, 1983; Milkereit & Starink, 2015; Strobel et al., 2019; Strobel, Easton, Sweet, Couper, & Nie, 2011; Strobel et al., 2016). Thus, the age hardenable aluminium alloys experience a solute loss due to this precipitation, and the formation of the strengthening precipitates during the subsequent artificial ageing is reduced. High strength alloys tend to be more quench sensitive, as the alloying elements provide a greater driving force for nucleation of non-strengthening precipitates during quenching (Strobel et al., 2011). While the dispersoids contribute significantly to the quench sensitivity of the alloys, they are wanted due to their ability to delay and hinder recrystallization during the thermo-mechanical processing, which is beneficial for the mechanical properties of the alloy (Remøe et al., 2017).

Whereas high strength alloys tend to be more quench sensitive, also lean alloys with few dispersoids have been observed to exhibit substantial quench sensitivity (Milkereit, Schick, & Kessler, 2010; Strobel et al., 2011; Strobel et al., 2016). Here the quench sensitivity has been linked to the supersaturation of vacancies, as the high number of vacancies after fast quenching leads to a possible increased rate of precipitate formation during artificial ageing (Deschamps et al., 2009; Evancho & Staley, 1974; Falahati, Lang, & Kozeschnik, 2012; Seyedrezai, Grebennikov, Mascher, & Zurob, 2009; Strobel et al., 2019; Werinos et al., 2016). This mechanism has also been found to affect quench sensitivity in alloys with a high content of dispersoids (Strobel et al., 2019).

Due to vacancy and/or solute diffusion, precipitate free zones (PFZs) form around dispersoids and grain boundaries in age hardenable aluminium alloys (Strobel et al., 2019, 2016; Unwin, Lorimer, & Nicholson, 1969). Since the PFZs lack strengthening precipitates, these zones are softer than the rest of the grain, but are typically stronger than pure aluminium as the PFZs retain some solute in solid solution (Unwin et al., 1969). The PFZs located adjacent to grain boundaries are the location and probably the cause of intercrystalline fracture (Lohne & Naess, 1979). Plastic deformation will localize in these weaker zones and crack initiation and growth can occur more easily in the PFZs (Chen, Pedersen, Clausen, & Hopperstad, 2009; Dowling & Martin, 1976; Khadyko, Marioara, Ringdalen, Dumoulin, & Hopperstad, 2016; Morgeneyer, Starink, Wang, & Sinclair, 2008). Due to this localization of deformation, the PFZs can develop significant misorientations relative to their parent grains, which in turn could contribute to the strengthening of the PFZs (Christiansen, Marioara, Marthinsen, Hopperstad, & Holmestad, 2018) and thus delay fracture initiation.

In general, a competition between intercrystalline and transcrystalline fracture is observed in age hardenable aluminium alloys. It has been reported that the fracture mode may change from transcrystalline to intercrystalline fracture due to the precipitation of coarse phases on grain boundaries and the formation of PFZs, which decrease the fracture toughness of the alloy (De Haas & De Hosson, 2002; Dumont, Deschamps, & Brechet, 2003, 2004a; Dumont, Deschamps, Bréchet, Sigli, & Ehrström, 2004b; Morgeneyer et al., 2008). As a result, fracture toughness may be significantly more sensitive to the quench rate than the strength of the alloy (Shuey, Tiryakioğlu, Bray, & Staley, 2006). Dumont et al. (2003, 2004a, 2004b) studied two 7000 series aluminium alloys using Kahn tear tests and found that a lower quench rate resulted in a lower fracture toughness, which was a result of the increased intercrystalline fracture caused by grain boundary precipitation and variations in the work-hardening rate. Morgeneyer et al. (2008) used synchrotron radiation computed tomography to study the failure mechanism ahead of the crack tip in Kahn tear tests for a 6000 series aluminium alloy. They found after a slow quench that fracture was mainly intercrystalline and that there was relatively little damage evolution prior to crack initiation.

In metallic materials, the mechanism for damage evolution and ductile fracture is nucleation, growth and coalescence of microscopic voids (Pineau, Benzerga, & Pardoen, 2016). Voids may nucleate at constituent particles or inclusions either by decohesion or by particle cracking (Maire, Zhou, Adrien, & Dimichiel, 2011), or voids may pre-exist in the material (Toda et al., 2013). Based on unit cell calculations using the finite element method (FEM), it has been found that damage evolution and ductile failure depend on a number of factors including the volume fraction of voids and particles, their distribution and shape, the plastic anisotropy, strength and work hardening of the matrix material, and on the local stress state (Pineau et al., 2016). Modelling of ductile materials is often done using micromechanically motivated homogenized material models such as porous plasticity models. In these models, the evolution of microstructural variables is included to describe effects such as material softening. These variables typically account for physical phenomena occurring at the lower

Table 1
Chemical compositions of the aluminium alloys in wt%.

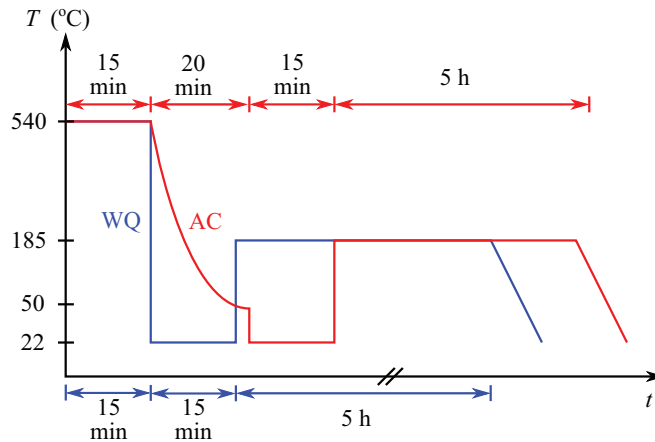| Alloy	Fe	Si	Mg	Mn	Cr	Cu	Zn	Ti	Al
6060	0.193	0.422	0.468	0.015	0.000	0.002	0.005	0.008	Bal.
6082.25	0.180	0.880	0.600	0.530	0.150	0.020	0.005	0.011	Bal.
6082.50	0.200	1.020	0.670	0.540	0.001	0.003	0.005	0.010	Bal.

Fig. 1. Heat-treatment of the alloys to temper T6, with either air-cooling (AC) or water-quenching (WQ) after the solution heat-treatment.

scales of ductile failure. The most renowned model based on this micromechanical framework, is the model proposed by Gurson (1977). This model is attractive due to its simple formulation, incorporating only a single microstructural parameter through the volume fraction of microscopic voids. The Gurson model has later been enhanced to give better agreement with unit cell calculations (Tvergaard, 1981) and extended to include effects such as void nucleation and coalescence (Tvergaard & Needleman, 1984). Versions of the model which take the plastic anisotropy of the matrix material into account have also been proposed (Dæhli, Faleskog, Børvik, & Hopperstad, 2017; Steglich, Wafai, & Besson, 2010).

In this study, the effect of quench rate on the plastic flow and fracture of age hardenable aluminium alloys is investigated. Using tensile tests on smooth and V-notch axisymmetric specimens, in addition to Kahn tear tests, the influence of stress state on the plastic flow and fracture of three AlMgSi alloys with different grain structure and crystallographic texture is determined. The alloys were solution heat-treated, cooled either in water or air to achieve different quench rates and artificially aged. It is found that the quench rate affects the precipitate structure of the alloys differently, and the slower cooling rate typically leads to wider PFZs around dispersoids and grain boundaries. These differences in microstructure are reflected in the mechanical behaviour of the materials. In addition, finite element simulations of the mechanical tests are performed for one of the alloys, using the Gurson (1977) model extended by Dæhli et al. (2017) to account for plastic anisotropy. Failure initiation is accurately captured in the finite element simulations, whereas the crack propagation energy in the simulations of the Kahn tear tests is somewhat overestimated.

2. Materials

Three aluminium alloys, namely 6060, 6082.25 and 6082.50, are studied experimentally. The chemical composition of the alloys is given in Table 1. The alloys were provided by Hydro Aluminium as extruded rectangular profiles with a thickness of 10 mm and a width of 83 mm. Three types of specimens were machined from the extruded profiles for mechanical testing, see Section 3.1.

All specimens were solution heat-treated and artificially aged to temper T6 (peak strength). After the solution heat-treatment, the specimens were cooled to room temperature using either air-cooling (AC) or water-quenching (WQ) to attain two different microstructures for each alloy, giving a total of six distinct materials. The solution heat-treatment consisted of keeping the specimens in a salt bath at 540 °C for 15 min, followed by either water-quenching to room temperature or air-cooling to 50 °C followed by water-quenching to room temperature. In the latter case, the temperature reached 50 °C after approximately 20 min with air-cooling. Subsequently, the specimens were stored at room temperature for 15 min before the artificial ageing to temper T6. To obtain the peak strength condition, the specimens were kept in an oil bath at 185 °C for five hours and then air-cooled to room temperature. Fig. 1 illustrates the temperature history of the specimens during the artificial ageing with either air-cooling or water-quenching after the solution heat-treatment. For each combination of
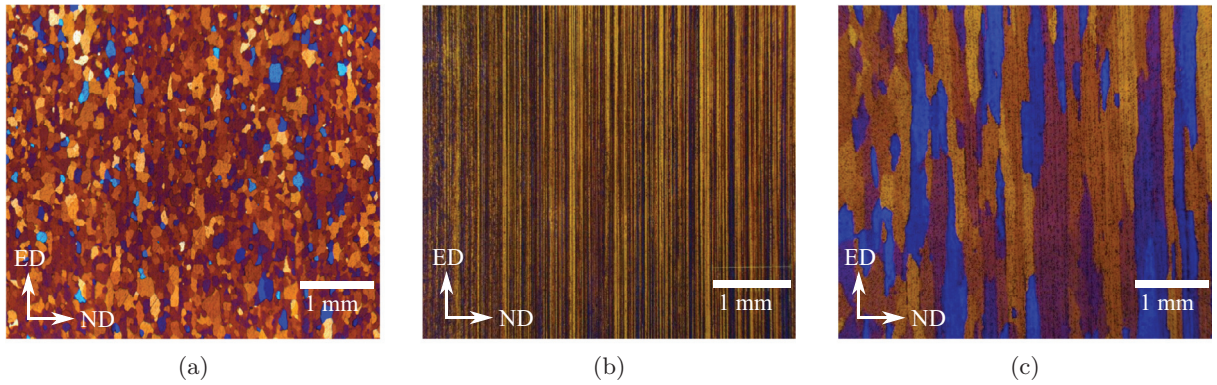
Fig. 2. Grain structure of the three alloys: (a) 6060, (b) 6082.25, and (c) 6082.50. Reprinted by permission from Springer Nature (Frodal et al., 2017).

specimen type and heat-treatment procedure, the temperature of one of the specimens was logged by a drilled-in thermo-couple.

The three aluminium alloys have different grain structure and crystallographic texture. The grain structure of the three alloys is shown in Fig. 2. The 6060 alloy has a recrystallized grain structure comprised of equiaxed grains of 60–70 µm and exhibits a cube texture with a minor Goss component. A typical fibrous, non-recrystallized grain structure is observed for the 6082.25 alloy, which has a cube texture with orientations along the β-fibre. These grains are several millimetres long in ED, approximately 150 µm in TD and 10 µm in the ND. In addition, the fibrous grain structure comprises sub-grains approximately 2–10 µm in diameter. The large elongated, recrystallized grains of the 6082.50 alloy exhibit a rotated cube texture, and are several millimetres long in ED, about 1–2 mm in TD and 300–400 µm in the ND (Frodal, Pedersen, Børvik, & Hopperstad, 2017).

For further details about the alloys, the reader is referred to Khadyko, Dumoulin, Børvik, and Hopperstad (2014), Frodal et al. (2017) and Christiansen et al. (2018).

3. Experimental procedures

3.1. Mechanical testing

In order to study the deformation and fracture mechanisms of these materials, different types of specimens were tested under quasi-static loading conditions, including cylindrical smooth and V-notch tensile specimens and Kahn tear test specimens. Fig. 3 shows the geometry of the three types of test specimens. The specimens were machined from the centre of the extruded profile. The tensile axis of the smooth and V-notch tensile specimens was oriented along the transverse direction (TD) of the profile. The Kahn tear test specimens were machined either with the tensile axis along the extrusion direction (ED) or along TD, and always perpendicular to the thickness direction (ND).

A displacement-controlled testing machine was used to perform the experiments, and a constant cross-head velocity of 1.00 mm/min, 0.12 mm/min and 1.00 mm/min were used for the tests on the smooth tensile specimens, the V-notch tensile specimens and the Kahn tear test specimens, respectively.

An in-house measuring system (Frodal et al., 2017) was used to measure the minimum diameters along ED and ND of the smooth and V-notch tensile specimens. The force and minimum diameters of the tensile specimen were continuously measured during the test until fracture. The current area of the minimum cross-section of the axisymmetric tensile specimen can be estimated by an elliptical area as

$$A = \frac{\pi}{4} D_1 D_3 \tag{1}$$

where D_1 and D_3 are the measured diameters in ED and ND, respectively. The true stress over the minimum cross-section area is then

$$\sigma_t = \frac{F}{A} \tag{2}$$

where F is the measured force. Assuming plastic incompressibility and negligible elastic strains, the logarithmic strain is given by

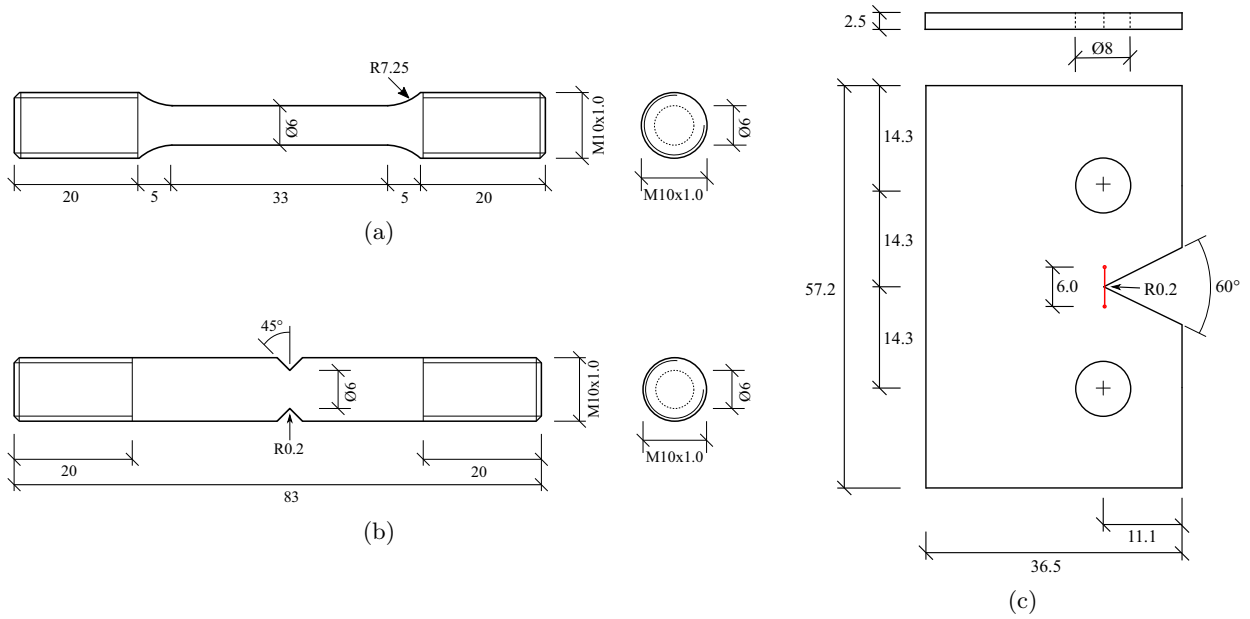$$\varepsilon_l = \ln \left(\frac{A_0}{A} \right) \tag{3}$$

Fig. 3. Geometry of the test specimens: (a) Smooth tensile specimen, (b) V-notch tensile specimen, and (c) Kahn tear test specimen with a red line indicating the virtual extensometer used. Dimensions in mm. (For interpretation of the references to colour in this figure legend, the reader is referred to the web version of this article.)

where A_0 is the initial cross-section area of the specimen. It is important to note that σ_t and ε_l represent average values over the minimum cross-section area of the tensile specimen.

In the Kahn tear tests, the force F and the cross-head displacement u were tracked continuously during testing. In addition, the displacement field on the surface of the specimen was obtained by digital image correlation (DIC). The displacement v across the crack tip of the Kahn test specimen was extracted using a virtual extensometer (Fig. 3c). In order to quantify the energy required to initiate and propagate a crack across the Kahn test specimen, the unit initiation energy (UIE) and unit propagation energy (UPE) were determined for each test. The UIE is calculated by

$$\text{UIE} = \frac{1}{bw} \int_0^{u_p} F \, du \tag{4}$$

where u_p is the displacement at peak force, b is the initial thickness, and w is the initial minimum width of the specimen. Similarly, the UPE is calculated by

$$\text{UPE} = \frac{1}{bw} \int_{u_p}^{u_f} F \, du \tag{5}$$

where u_f is the displacement where the force has dropped to 1% of the maximum force (ASTM, 2001). These energy measures can provide useful insight when investigating a material's resistance to crack growth, as both strength and ductility are considered.

Three tests were conducted for each combination of specimen type, tensile direction and material, i.e., alloy and cooling rate (air-cooling or water-quenching) after the solution heat-treatment. Hence, a total of 18 tensile tests on smooth specimens, 18 tensile tests on V-notch specimens, and 36 Kahn tear tests were conducted.

3.2. Microstructure characterization

Undeformed samples were anodized at room temperature for 2 min using HBF_4 (Fluoroboric acid) to reveal the grain structure under polarized light in the optical microscope. Fracture surfaces of the failed V-notch and Kahn tear test specimens were investigated in a Zeiss Gemini Supra 55VP FESEM operated at 20 kV.

Precipitation in the different alloys was characterized using transmission electron microscopy (TEM). Thin foils of the materials were prepared using conventional thin foil preparation procedures. Sections from the undeformed regions of the Kahn tear test specimens were cut using an automated high-speed saw. These sections were then polished down to ≈ 300 μm before 3 mm diameter disks were punched out and further polished down to ≈ 100 μm thickness with a mirror-like finish. A twin-jet Struers TenuPol 3 electropolishing system operated at 20 V was used to electropolish the disks and provide electron transparent regions for TEM investigations. The electrolyte consisted of 1/3 HNO_3 (nitric acid) and 2/3 CH_3OH (methanol), and was kept at $\approx -25 \pm 5$ °C during the process. Reliable TEM investigations of precipitation require the thin foil surface
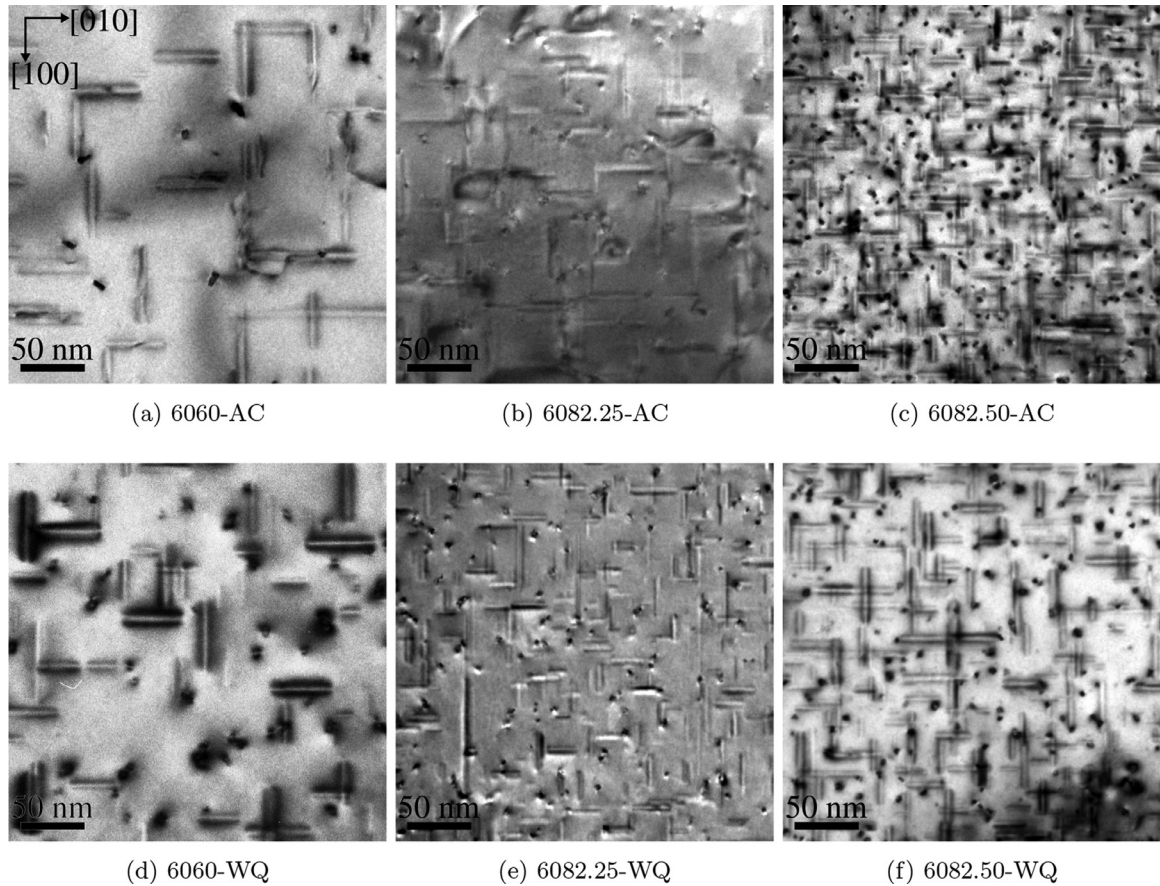
Fig. 4. TEM [001] zone axis bright field images of precipitation in (a-c) air-cooled and (d-f) water-quenched undeformed materials. The imaged areas are of comparable thickness and identical scale. Precipitates oriented along [100] and [010] matrix crystallographic directions, i.e., lying in the paper plane, are visible through the dark strain field in the surrounding matrix. Precipitates oriented along [001], i.e., out of the paper plane, appear as black dots. Differences in contrast and precipitate appearance are largely due to different specimen tilt and diffraction conditions.

normal to be close to a ⟨001⟩ direction, i.e., a [001] zone axis is desired at relatively low specimen tilt. Because the thin foil preparation technique produces specimens with an inherent variation in quality and the thin areas of the final foils might not contain any grains with a [001] zone axis, several thin foils from each specimen were prepared. In the 6082.50 alloy, this was especially challenging due to the abnormally large grains, and electron backscattering in the scanning electron microscope (SEM) was used to select sections from the Kahn test specimens. Before TEM investigations, the finished thin foils were cleaned for $\approx$ 3 min in a Fischione 1020 Plasma Cleaner.

TEM investigations were carried out on two different instruments. The water-quenched 6060 alloy was characterized on a Philips CM30 with a LaB$_6$ filament operated at 150 kV in a previous study (Christiansen et al., 2018). The remaining materials were characterized on a JEOL JEM2100 with a LaB$_6$ operated at 200 kV. The thickness of the imaged areas in the thin foils was measured by electron energy loss spectroscopy (EELS), using a Gatan PEELS model 601 on the CM30 microscope and a Gatan Imaging Filter system on the JEM2100 microscope. Precipitation in the different materials was evaluated by measuring the average needle length, cross-sectional area, number density, and volume fraction, following the procedure of Andersen (1995) and Marioara, Andersen, Zandbergen, and Holmestad (2005). In 6000 series aluminium alloys close to peak hardness, most of the precipitates will be of the needle-shaped β'' phase, although Cu-containing alloys will likely contain some Q' and L phases as well (Sunde, Marioara, van Helvoort, & Holmestad, 2018). Most precipitates will therefore have identical shapes and it is possible to estimate the average size, number density, and volume fraction of precipitates given measured needle lengths, cross-sections, and number densities.

4. Experimental results

4.1. Initial microstructure

Fig. 4 shows TEM bright field images of the undeformed materials. Air-cooling has an adverse effect on precipitation in all alloys, but the precipitate microstructure of the alloys is differently affected. The 6060 alloy develops slightly coarser
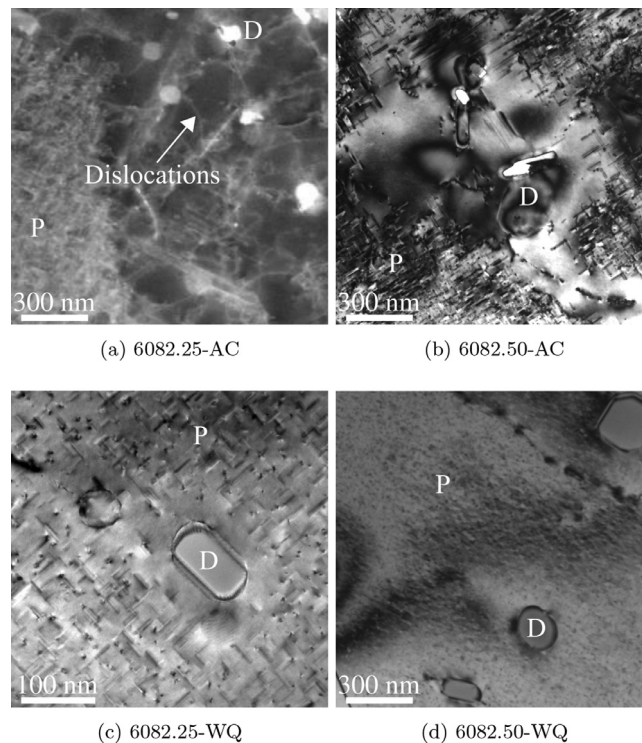
Fig. 5. TEM images of precipitation (marked "P") around dispersoids (marked "D") in the dense 6082 alloys after air-cooling (a,b), and after water-quench (c,d). The image in subfigure (a) is a medium-angle annular dark field scanning TEM (STEM) image, while the other images are TEM bright field images. The reason for applying STEM is that the air-cooled condition of 6082.25 contains many dislocations, as indicated, and their strain fields dominate the bright field contrast. Note the difference in scale between subfigure (c) and the other images.

precipitates, which are more sparsely distributed after air-cooling. In the 6082.25 alloy, precipitation becomes very inhomogeneous and is limited to small regions that contain slightly larger precipitates compared to the water-quenched condition. The 6082.50 alloy also exhibits inhomogeneous precipitation after air-cooling, but not to the same degree as the 6082.25 alloy. Where precipitates have formed in the air-cooled 6082.50 alloy, the local number density is greater and the precipitates are smaller, compared to the water-quenched condition. Fig. 5 presents TEM images of the dispersoids responsible for the inhomogeneous precipitation in the two 6082 alloys. Air-cooling causes dispersoids to nucleate large precipitates and drain their neighbouring region of solute, suppressing precipitation of strengthening precipitates. Because the number density of dispersoids in the 6082.25 alloy is greater than in the 6082.50 alloy, the PFZs around dispersoids and grain boundaries (GBs) overlap, resulting in PFZs that span entire grains and leave only a few regions of sparse precipitation. Dislocations observed in the PFZs of this alloy are probably generated due to the constraint that are introduced by the growth of large precipitates nucleated on dispersoids. In the 6082.50 alloy, the dispersoid density is substantially lower, so that strengthening precipitates may form in regions situated a certain distance from each dispersoid. Grain boundary PFZs are also changed by the cooling rate. Fig. 6 presents representative TEM bright field images of grain boundary regions and surrounding PFZs. The observed trend is that the slow cooling rate leads to wider PFZs around grain boundaries, similar to the trend of PFZs around dispersoids.

Table 2 summarises the TEM observations, where average numbers for needle length, cross-sectional area, number density, and volume fractions are presented, along with approximate PFZ widths. Precipitate statistics were not performed for the air-cooled 6082.25 alloy, due to its severely inhomogeneous precipitate microstructure. Note that the reported number density for the air-cooled 6082.50 alloy is an overestimate of the average number density, as it is estimated based on the dense precipitation regions. The PFZs around GBs and dispersoids will reduce the actual number density and volume fraction of precipitates in this alloy after air-cooling.

The main result from the TEM study is that air-cooling reduces the total number density and volume fraction of strengthening precipitates in all the studied alloys. Preciptiation is less affected by the cooling rate in the 6060 alloy, and most affected in the 6082.25 alloy where it is almost entirely suppressed. In the 6082.50 alloy, air-cooling results in very dense precipitation of fine precipitates and large PFZs around dispersoids scattered throughout the grains. This means that the precipitation microstructure of the 6082.50 alloy becomes inhomogeneous, with soft regions (dispersoids with PFZs) dispersed in a strong matrix (preciptiate strengthened regions), where the strong matrix has a strength comparable to the water-quenched state.
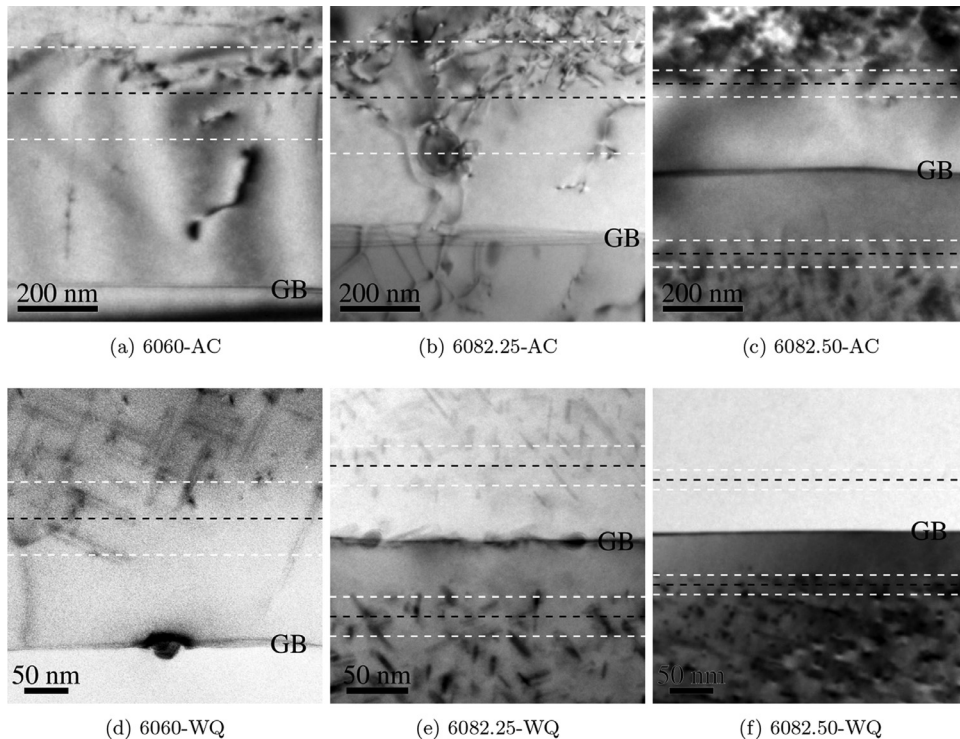
Fig. 6. TEM bright field images of grain boundaries (marked by "GB") and surrounding PFZs in (a–c) air-cooled and (d–f) water-quenched materials. Black dashed lines mark the PFZ width, while the white dashed lines mark the estimated error of the PFZ width. The scale in subfigures (a–c) is the same, but for subfigures (d–f) the scale is larger for subfigure (e) than for subfigures (d) and (f).

Table 2
Average estimates of precipitation in the alloys. Precipitation in the air-cooled 6082.25 alloy is inhomogeneous, and no statistics are available.

Material	Needle length (nm)	Needle cross-section (nm^2)	Number density (#/µm^3)	Volume fraction (%)	PFZ width (nm)
6060-AC	41.8 ± 2.4	23.4 ± 4.2	2839 ± 272	0.27 ± 0.02	478 ± 114
6060-WQ	40.0 ± 1.0	19.1 ± 0.8	5556 ± 629	0.42 ± 0.05	146 ± 41
6082.25-AC	–	–	–	–	334 ± 138[b]
6082.25-WQ	22.9 ± 0.6	7.0 ± 0.3	40232 ± 3563	0.64 ± 0.05	61 ± 16
6082.50-AC	26.5 ± 0.5	8.3 ± 0.3	53870 ± 3826[a]	1.18 ± 0.08	211 ± 33
6082.50-WQ	32.1 ± 2.3	10.2 ± 0.5	42183 ± 7534	1.26 ± 0.14	59 ± 11

[a] The precipitation statistics for the air-cooled 6082.50 alloy are from dense precipitate regions, and the number density does not reflect the inhomogeneous precipitate microstructure.

[b] PFZs usually span entire grains.

4.2. Mechanical response

4.2.1. Tensile tests on smooth and V-notch specimens

Fig. 7 presents the true stress-strain curves from the tensile tests on smooth specimens plotted up to failure. Three parallel tests were performed for each material. Only two repeat tests were successful for the water-quenched and air-cooled 6082.50 alloy, as the other specimens failed close to the grip section. Comparing the two heat-treatments, it is obvious that the strength is lower with air-cooling than with water-quenching for all the alloys. The strain to failure is greater with air-cooling than with water-quenching for the 6060 and 6082.25 alloys. For the 6082.50 alloy, a large scatter is observed in the failure strain for the water-quenched material, and the failure strain for the air-cooled material is within this range. The scatter is caused by the large grains of this alloy, as the number of grains across the specimen diameter is small. Relatively little scatter is observed for the other materials. For the water-quenched materials, the initial yield stress is the lowest for the 6060 alloy, while the two 6082 alloys have a higher and similar initial yield stress, with the 6082.25 alloy a little higher than the 6082.50 alloy. With air-cooling, the initial yield stress of the 6082.25 alloy is the lowest, and the initial yield stress of the 6060 alloy is between the two 6082 alloys. Thus, the largest difference in strength due to the heat-treatment is observed for the 6082.25 alloy, see Table 3.
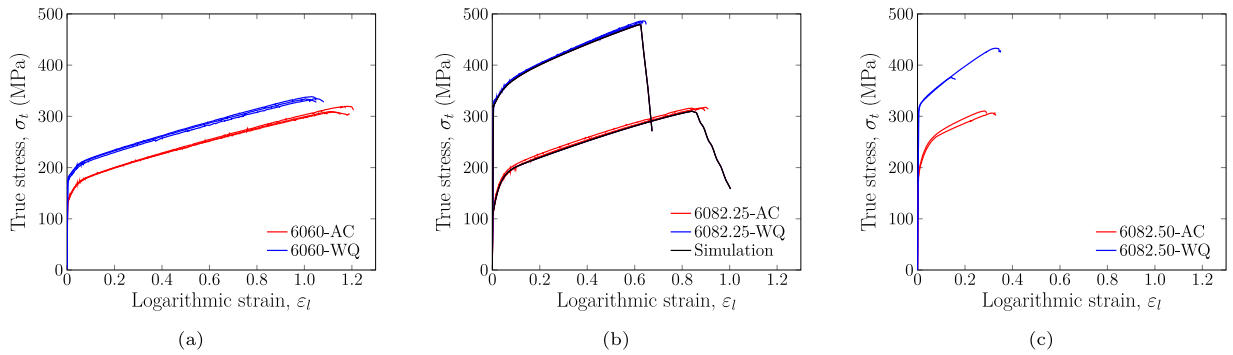
Fig. 7. Stress-strain curves from the tensile tests on smooth specimens: (a) 6060, (b) 6082.25, and (c) 6082.50. Simulation results are shown for the 6082.25 alloy.

Table 3
Initial yield stress at 0.2% plastic strain, $\sigma_{0.2}$, from the smooth tensile tests, with standard deviations.

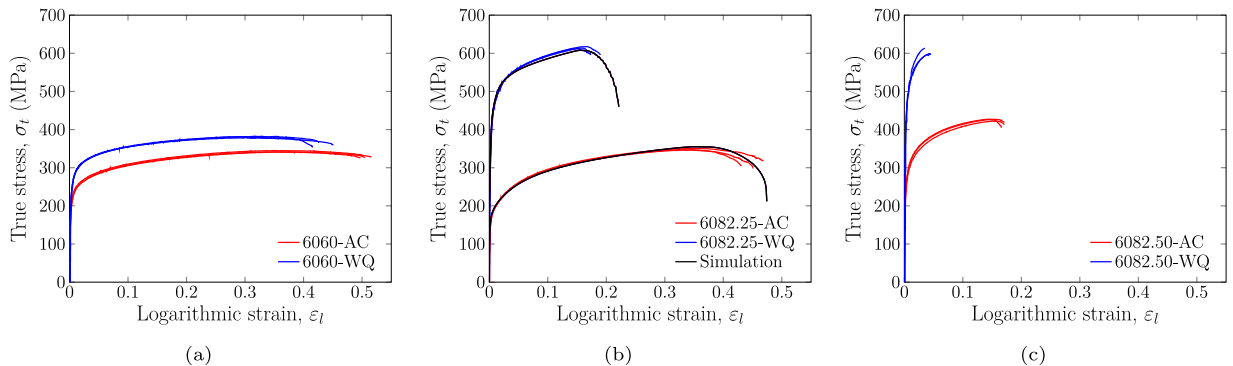| Material	$\sigma_{0.2}$ (MPa)
6060-AC	132.6 ± 0.5
6060-WQ	176.4 ± 2.7
6082.25-AC	113.4 ± 3.0
6082.25-WQ	327.7 ± 0.5
6082.50-AC	179.5 ± 6.4
6082.50-WQ	315.0 ± 1.3

Fig. 8. Stress-strain curves from the tensile tests on V-notch specimens: (a) 6060, (b) 6082.25, and (c) 6082.50. Simulation results are shown for the 6082.25 alloy.

The stress-strain curves up to failure from the tensile tests on V-notch specimens are presented in Fig. 8. Three repeat tests are shown for each material and the scatter is small. It is evident that the stress level is elevated in the V-notch specimens compared to the smooth specimens due to the notch strengthening effect, which is caused by the triaxial stress field in the notch. Similar trends are observed here as in Fig. 7, but the failure strain is clearly lower with water-quenching than with air-cooling in the tensile tests on the V-notch specimens—and this holds for the 6082.50 alloy as well. By comparison of Figs. 7 and 8, it is found that the failure strain is substantially lower in the tensile tests on V-notch specimens, due to the increased stress triaxiality induced by the sharp notch.

Lankford coefficients measured in the tensile tests on smooth and V-notch specimens are given in Table 4. These coefficients give the ratio between the incremental strains in ED and ND, and thus represent the evolution of the cross-section of the specimen with plastic deformation. Small variations in the Lankford coefficients are observed between the materials with the different cooling rates. For the 6060 and 6082.50 alloys, the air-cooled materials appear to be slightly less anisotropic than the water-quenched materials, in the sense that the Lankford coefficient is closer to unity, whereas the opposite trend is found for the 6082.25 alloy. The Lankford coefficients obtained from the tensile tests on the smooth and V-notch specimens are similar for the two 6082 alloys, while the coefficients for the 6060 alloy are markedly lower in the V-notch specimens. The latter observation indicates that the plastic flow is strongly influenced by the triaxial stress field imposed by the sharp notch.

Table 4
Measured Lankford coefficients from the smooth and V-notch tensile tests, with standard deviations.

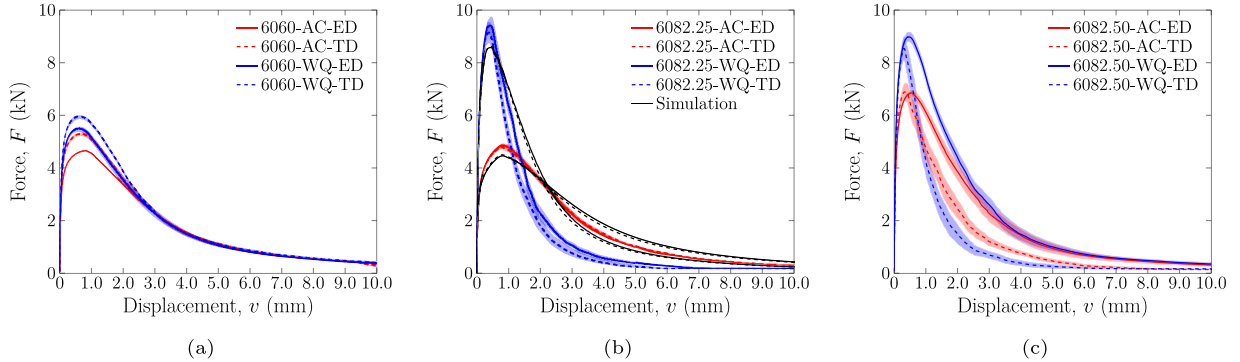| Material	Smooth	V-notch
6060-AC	3.67 ± 0.07	1.94 ± 0.15
6060-WQ	3.95 ± 0.11	2.04 ± 0.25
6082.25-AC	0.84 ± 0.00	0.81 ± 0.01
6082.25-WQ	1.10 ± 0.01	0.94 ± 0.01
6082.50-AC	0.32 ± 0.09	0.35 ± 0.04
6082.50-WQ	0.19 ± 0.05	0.22 ± 0.06

Fig. 9. Force-displacement curves from the Kahn tear tests showing the mean curve with the scatter in shaded colour: (a) 6060, (b) 6082.25, and (c) 6082.50. Simulation results are shown for the 6082.25 alloy.

Table 5
Unit initiation energy (UIE) and unit propagation energy (UPE) from the Kahn tear tests, with standard deviations.

Material	UIE (kJ/m^2)		UPE (kJ/m^2)	
	ED	TD	ED	TD
6060-AC	94.0 ± 0.7	102.5 ± 4.0	231.0 ± 2.0	250.0 ± 7.1
6060-WQ	87.8 ± 7.7	109.2 ± 1.8	249.2 ± 8.1	267.2 ± 0.9
6082.25-AC	144.7 ± 2.7	132.5 ± 5.8	213.1 ± 1.1	218.0 ± 3.2
6082.25-WQ	147.6 ± 9.9	135.5 ± 9.5	145.1 ± 9.1	118.2 ± 16.0
6082.50-AC	115.9 ± 3.5	81.6 ± 3.9	244.8 ± 24.6	153.6 ± 16.7
6082.50-WQ	128.3 ± 5.1	98.9 ± 5.1	276.2 ± 18.5	101.5 ± 3.7

4.2.2. Kahn tear tests

Fig. 9 displays the force-displacement curves from the Kahn tear tests. The virtual extensometer situated across the notch tip, depicted in Fig. 3c, is used to obtain a measure of the notch tip opening displacement. The differences in strength of the air-cooled and water-quenched materials observed in the tensile tests on smooth and V-notch specimens are also seen here. The peak force is consistently lower for the air-cooled than for the water-quenched materials, and thus crack initiation always occurs at a lower force for the former materials. Variations between the two loading directions are also observed. For the 6060 alloy, the test in the transverse direction (TD) has the highest peak force, whereas the test in the extrusion direction (ED) has the highest peak force for the two 6082 alloys. For the 6082.50 alloy, tests along ED give markedly higher ductility than tests along TD, while the difference for the 6082.25 alloy is small. This large difference in ductility with loading direction is attributed to the grain structure of the 6082.50 alloy. The large elongated grains of this alloy, which are several millimetres along ED (Frodal et al., 2017), make the material more susceptible to intercrystalline fracture when loaded along TD, see Section 4.3.

Table 5 presents the unit initiation energies (UIEs) and unit propagation energies (UPEs) calculated based on the Kahn tear tests, see Eqs. (4) and (5). Here, the cross-head displacement has been used to calculate these energies in accord with ASTM (2001). The UIE and UPE are the energies per unit area required to initiate crack growth and propagate a crack through the material, respectively. Similar values of the UIE are found for the same alloy and loading direction. Albeit the force level is significantly lower for the air-cooled materials than for the water-quenched materials, the UIEs are similar, indicating that the displacement to crack initiation is larger for the air-cooled materials.

The UPE is greater for the water-quenched material than for the air-cooled material in both loading directions for the 6060 alloy, suggesting that the water-quenched material has a higher resistance to crack propagation. This trend is reversed for the 6082.25 alloy, and the air-cooled material has the greatest propagation energy in both loading directions. For the
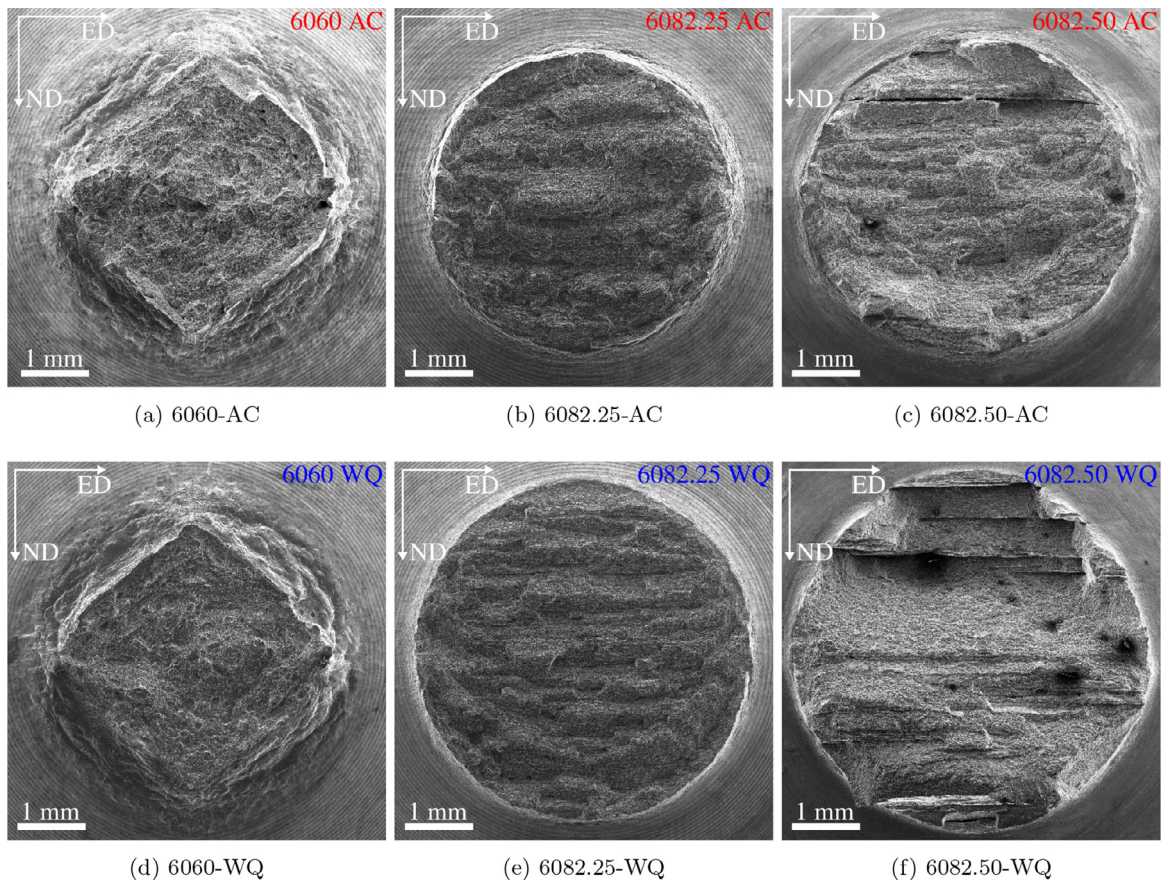
Fig. 10. Fracture surfaces of the V-notch tensile specimens for the three alloys with air-cooling, AC (top) and water-quenching, WQ (bottom).

6082.50 alloy, the loading direction has a substantial effect on the UPE, and this effect is greater for the water-quenched material than for the air-cooled material. The result is that for the 6082.50 alloy, the water-quenched material has the highest UPE in ED, whereas the air-cooled material has the highest UPE in TD.

4.3. Fractography

To get a deeper understanding of the mechanisms involved in the fracture process, a fractographic analysis of the tested specimens is performed in the SEM. Fig. 10 presents the fracture surfaces of the V-notch tensile specimens for the three alloys with air-cooling and water-quenching. Three distinct fracture surface shapes are observed, where each alloy exhibits a distinct shape. The 6060 alloy displays a flat diamond-shaped fracture surface. A flat circular cross-section is recognized for the 6082.25 alloy, whereas the 6082.50 alloy demonstrates a slant circular fracture surface which is a result of the large grains. The diamond-shaped fracture surface found for the 6060 alloy is caused by the strong cube texture in combination with the superimposed triaxial stress field of the V-notch specimen (Khadyko, Dumoulin, Børvik, & Hopperstad, 2015). This diamond-shaped cross-section will yield inaccuracies in the logarithmic strain measure, defined by Eq. (3), for large deformations, as the area calculation used in the strain measure is based on an assumption of an elliptical minimum area, see Eq. (1).

Fracture is mainly transcrystalline for the 6060 and 6082.25 alloys, with some areas of intercrystalline fracture. In contrast, the 6082.50 alloy has substantial amounts of intercrystalline fracture, see also Figs. 11, , and–13. In general, the same fracture surface shapes and fracture modes are observed for the air-cooled and water-quenched materials in Fig. 10. The air-cooled materials have smaller fracture areas than the water-quenched materials, in agreement with larger fracture strains, see Section 4.2.1. For the 6060 and 6082.25 alloys, the fracture is mainly transcrystalline for both the air-cooled and the water-quenched materials, whereas the amount of intercrystalline fracture is greater for the water-quenched material than for the air-cooled material for the 6082.50 alloy.

Fig. 11 shows the fracture surfaces of the Kahn tear test specimens for the 6060 alloy, including the two loading directions and the air-cooled and water-quenched materials. The fracture surfaces are clearly distinct and variations are seen between the two loading directions and the two cooling rates. For the materials loaded along ED, transcrystalline fracture
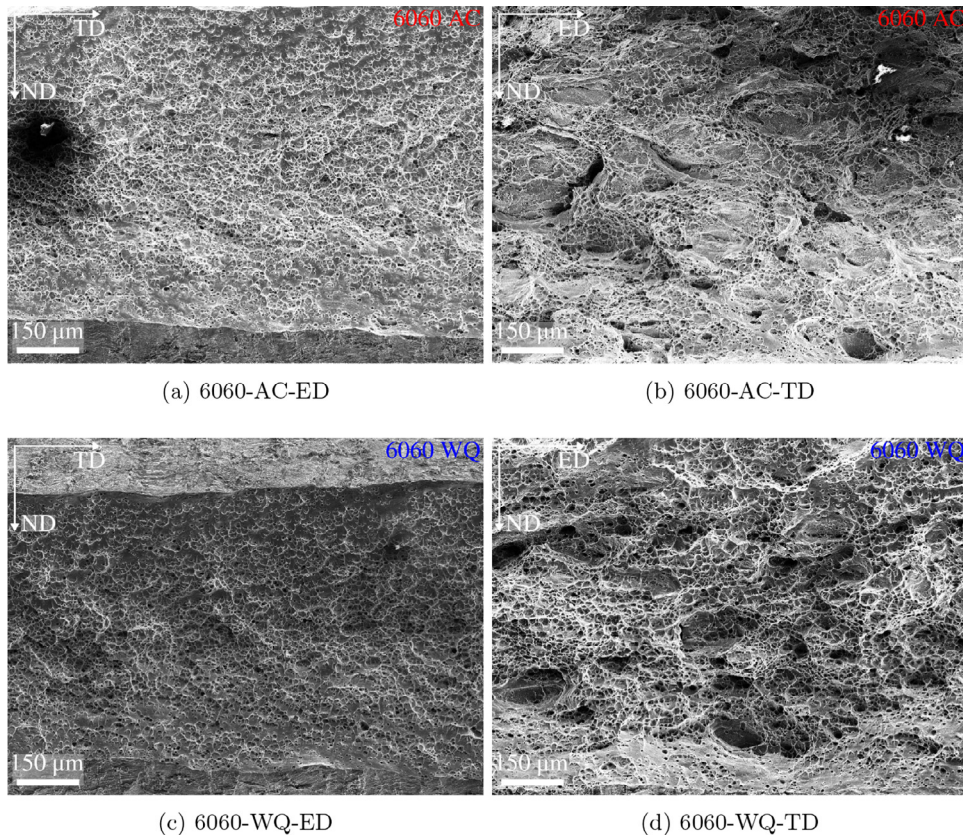
(a) 6060-AC-ED

(b) 6060-AC-TD

(c) 6060-WQ-ED

(d) 6060-WQ-TD

Fig. 11. Fracture surfaces of the Kahn tear test specimens for the 6060 alloy.

is dominant. In contrast, along TD a considerable amount of the fracture surface is covered with areas of intercrystalline fracture. As this alloy has equiaxed grains, the more probable cause of this difference is the crystallographic texture. The Goss texture component is likely to cause greater imbalance and stress concentrations between grains when loaded along TD, leading to highly localized deformation in the PFZs and along grain boundaries. This will in turn lead to different behaviours along different material orientations as observed for loading along ED and TD. Comparing the different cooling rates it is evident that the width of the fracture area for the water-quenched material is smaller than that for the air-cooled material loaded along ED, suggesting that the water-quenched material has a greater ductility. For the specimens loaded along ED, the fracture surfaces of the air-cooled and water-quenched materials are similar, displaying similar dimple structures. A greater difference is observed between the two cooling rates for the specimens loaded along TD. The air-cooled material has a larger amount of intercrystalline fracture than the water-quenched material, again suggesting that the water-quenched material has a greater ductility.

Fig. 12 depicts the fracture surfaces of the Kahn specimens for the 6082.25 alloy, including the two cooling rates and the two loading directions. The fracture surfaces are similar in all these cases. Transcrystalline fracture is dominant with only minor intercrystalline fracture, i.e., some areas of intercrystalline fracture can be seen between the large areas filled with dimples formed in the grain interior.

The fracture surfaces of the Kahn specimens for the 6082.50 alloy, including the two cooling rates and the two loading directions, are shown in Fig. 13. In contrast to the 6082.25 alloy, the 6082.50 alloy clearly shows distinct fracture surfaces for the different cases. For the tests loaded along ED, only transcrystalline fracture is seen for the water-quenched material. In contrast, large areas of intercrystalline fracture are observed for the air-cooled material, indicating a failure mode with lower ductility than for the water-quenched material. Larger amounts of intercrystalline fracture are observed for the Kahn specimens loaded along TD due to the grain structure of this alloy. The large elongated grains, see Fig. 2, make the material less susceptible to intercrystalline fracture in ED as the fracture path is forced through the grains by the notch of the Kahn specimen. The ratio of intercrystalline to transcrystalline fracture for the specimens loaded along TD appears to be larger for the water-quenched material than for the air-cooled material. Thus, different trends of intercrystalline fracture are seen for the two loading directions. This indicates that for loading along ED, the water-quenched material is the most ductile, whereas it is the air-cooled material that is the most ductile when loaded along TD, in agreement with Table 5.

(a) 6082.25-AC-ED

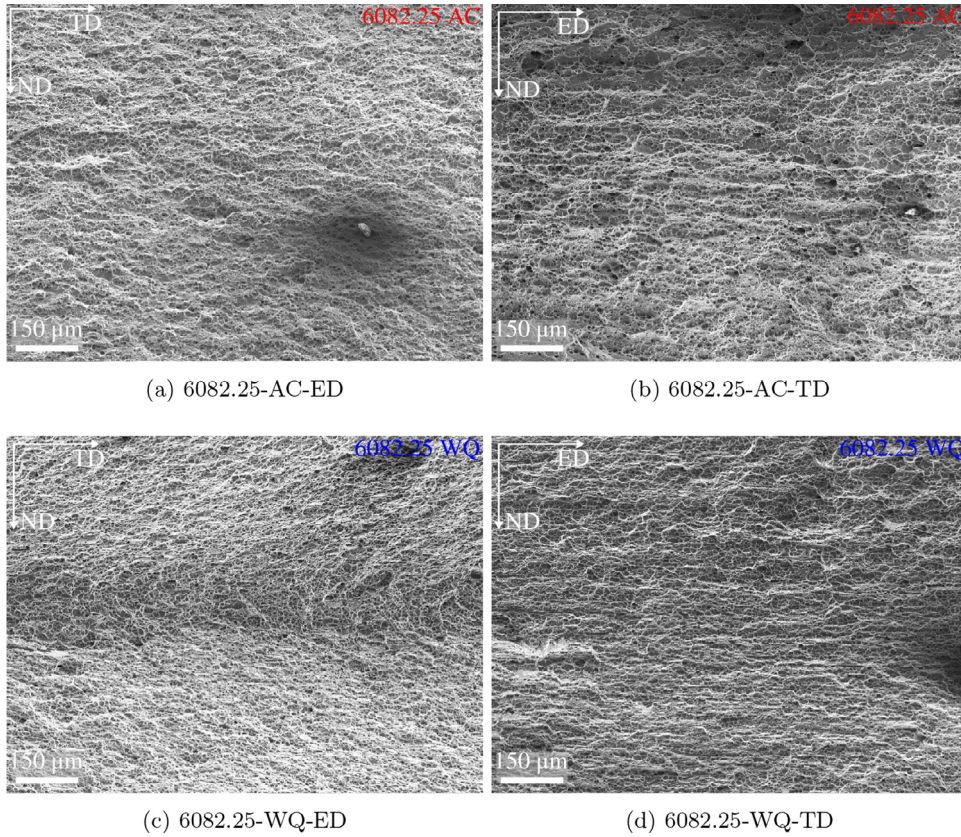(b) 6082.25-AC-TD

(c) 6082.25-WQ-ED

(d) 6082.25-WQ-TD

Fig. 12. Fracture surfaces of the Kahn tear test specimens for the 6082.25 alloy.

Constituent particles can be seen at the bottom of many of the dimples for all materials, indicating ductile fracture involving nucleation, growth and coalescence of voids. Voids may be nucleated from constituent particles either by decohesion or by particle cracking (Maire et al., 2011), or may pre-exist in the materials (Toda et al., 2013). The 6060 alloy contains constituent particles of type AlFeSi, while the two 6082 alloys contain constituent particles of type AlFeSiMn, and the particles are larger in the two 6082 alloys than in the 6060 alloy (Frodal et al., 2017). Cracked particles can be found at the bottom of some dimples. These particles cracked during the extrusion process, and fully or partially cracked particles can be found in undeformed samples (Frodal et al., 2017). In some areas, intercrystalline fracture with a high density of smaller dimples is revealed, and it is reasonable to assume that these dimples are caused by void growth within the PFZ, possibly nucleated at grain boundary precipitates (Chen et al., 2009).

5. Numerical study

5.1. Constitutive model

In this section, the constitutive relations of the porous plasticity model, which is used in the subsequent finite element simulations of some of the tests, are outlined. It is assumed that the elastic deformations are infinitesimal, while plastic deformations and rotations may be finite. The physical mechanisms of damage evolution and failure are growth and coalescence of voids in the ductile matrix material. A corotational formulation of the anisotropic porous plasticity model is used, and the components of the Cauchy stress tensor and the rate of deformation tensor are expressed in a co-rotated coordinate system by

$$\hat{\sigma}_{ij} = R_{ki}\sigma_{kl}R_{lj} \quad \wedge \quad \hat{D}_{ij} = R_{ki}D_{kl}R_{lj} \tag{6}$$

where **R** is the rotation tensor from the polar decomposition of the deformation gradient **F**. The rate of deformation tensor **D** is additively decomposed into elastic and plastic parts

$$\hat{D}_{ij} = \hat{D}^e_{ij} + \hat{D}^p_{ij} \tag{7}$$

(a) 6082.50-AC-ED

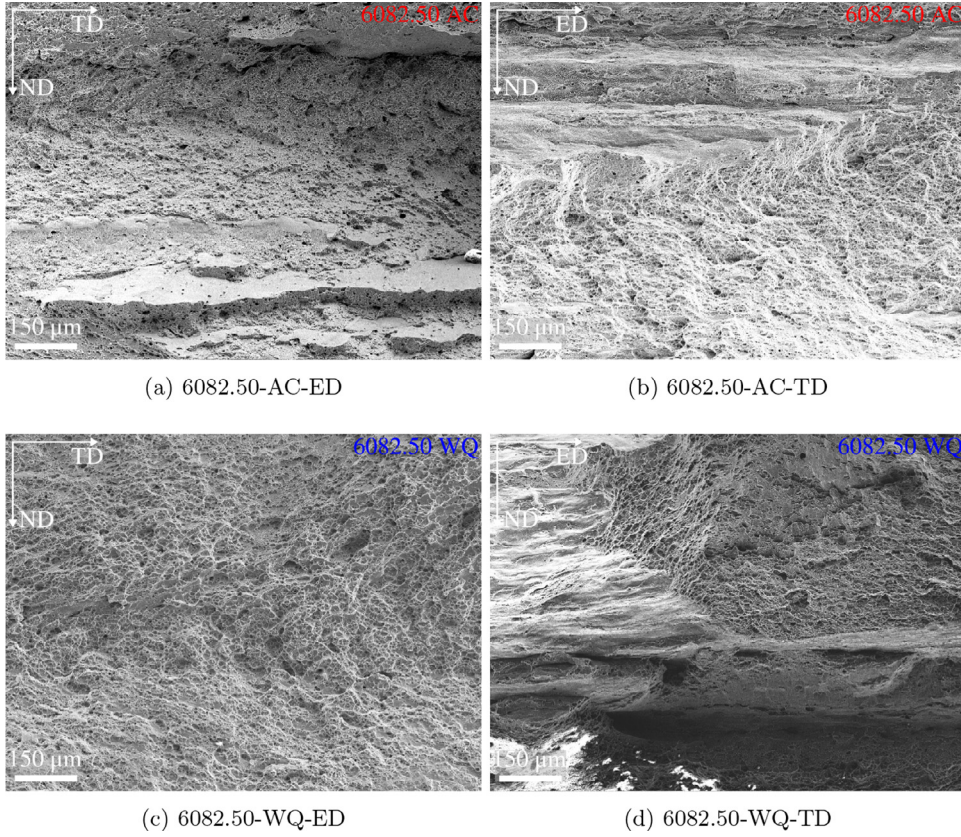(b) 6082.50-AC-TD

(c) 6082.50-WQ-ED

(d) 6082.50-WQ-TD

Fig. 13. Fracture surfaces of the Kahn tear test specimens for the 6082.50 alloy.

where $\mathbf{D}^e$ and $\mathbf{D}^p$ are the elastic and plastic rate of deformation tensors, respectively. In the co-rotated coordinate system, the rate form of the generalized Hooke's law can be expressed as

$$\dot{\hat{\sigma}}_{ij} = \frac{E}{1+\nu}\hat{D}_{ij}'^e + \frac{E}{3(1-2\nu)}\hat{D}_{kk}\delta_{ij} \tag{8}$$

where $\mathbf{D}'^e$ is the deviatoric part of the elastic rate of deformation tensor, δ_{ij} is the Kronecker delta, and E and ν are Young's modulus and Poisson's ratio, respectively.

Plastic yielding is governed by the heuristic extension of the Gurson-Tvergaard-Needleman model (Gurson, 1977; Tvergaard, 1981; Tvergaard & Needleman, 1984) proposed by Dæhli et al. (2017), and the yield function takes the form

$$\Phi(\boldsymbol{\sigma}, p, f) = \left(\frac{\varphi(\boldsymbol{\sigma})}{\sigma_y}\right)^2 + 2q_1 f^* \cosh\left(\frac{q_2 \hat{\sigma}_{kk}}{2\sigma_y}\right) - 1 - (q_1 f^*)^2 \leq 0 \tag{9}$$

where σ_y is the matrix flow stress, f^* is the effective void volume fraction introduced by Tvergaard and Needleman (1984), and q_i are the model parameters suggested by Tvergaard (1981). As in the original Gurson (1977) model, the growing voids are assumed to be spherical in shape. The equivalent stress φ is now defined by the Yld2004-18p model proposed by Barlat et al. (2005), which accounts for the plastic anisotropy of the matrix material, as

$$\varphi(\boldsymbol{\sigma}) = \left(\frac{1}{4}\sum_{k=1}^{3}\sum_{l=1}^{3}\left|S_k^{(1)} - S_l^{(2)}\right|^a\right)^{\frac{1}{a}} \tag{10}$$

where a is an exponent determining the curvature of the yield surface, and $S_k^{(1)}$ and $S_l^{(2)}$ are the principal values of the tensors $\mathbf{s}^{(1)}$ and $\mathbf{s}^{(2)}$, respectively. The tensors $\mathbf{s}^{(1)}$ and $\mathbf{s}^{(2)}$ are determined by the linear transformations

$$\hat{s}_{ij}^{(1)} = \hat{\mathbb{C}}_{ijkl}^{(1)}\hat{\sigma}_{kl}' \quad \wedge \quad \hat{s}_{ij}^{(2)} = \hat{\mathbb{C}}_{ijkl}^{(2)}\hat{\sigma}_{kl}' \tag{11}$$

where $\boldsymbol{\sigma}'$ is the deviatoric part of the Cauchy stress tensor, and the fourth-order tensors $\mathbb{C}^{(1)}$ and $\mathbb{C}^{(2)}$ contain coefficients describing the plastic anisotropy (Barlat et al., 2005; Dæhli et al., 2017). For an orthotropic material, Eq. (11) can be written

on matrix form as

$$
\begin{bmatrix} \hat{s}_{11}^{(k)} \\ \hat{s}_{22}^{(k)} \\ \hat{s}_{33}^{(k)} \\ \hat{s}_{12}^{(k)} \\ \hat{s}_{23}^{(k)} \\ \hat{s}_{31}^{(k)} \end{bmatrix} = \begin{bmatrix} 0 & -\hat{c}_{12}^{(k)} & -\hat{c}_{13}^{(k)} & 0 & 0 & 0 \\ -\hat{c}_{21}^{(k)} & 0 & -\hat{c}_{23}^{(k)} & 0 & 0 & 0 \\ -\hat{c}_{31}^{(k)} & -\hat{c}_{32}^{(k)} & 0 & 0 & 0 & 0 \\ 0 & 0 & 0 & \hat{c}_{44}^{(k)} & 0 & 0 \\ 0 & 0 & 0 & 0 & \hat{c}_{55}^{(k)} & 0 \\ 0 & 0 & 0 & 0 & 0 & \hat{c}_{66}^{(k)} \end{bmatrix} \begin{bmatrix} \hat{\sigma}_{11}' \\ \hat{\sigma}_{22}' \\ \hat{\sigma}_{33}' \\ \hat{\sigma}_{12}' \\ \hat{\sigma}_{23}' \\ \hat{\sigma}_{31}' \end{bmatrix} \quad k = 1, 2 \tag{12}
$$

where the 18 non-zero anisotropy parameters $\hat{c}_{ij}^{(1)}$ and $\hat{c}_{ij}^{(2)}$ together with the exponent a determine the shape of the yield surface in stress space. Recently, van den Boogaard, Havinga, Belin, and Barlat (2016) showed that the 18 anisotropy parameters can be reduced to 16 independent ones. Thus, we will select $\hat{c}_{12}^{(1)} = \hat{c}_{13}^{(1)} = 1$. Any other choice will give equivalent results, but for an isotropic material these selected values will result in that all $\hat{c}_{ij}^{(1)}$ and $\hat{c}_{ij}^{(2)}$ become equal to one and that $\varphi(\boldsymbol{\sigma})$ reduces to the Hershey–Hosford equivalent stress. The associated flow rule is used, and the plastic rate of deformation tensor reads

$$
\hat{D}_{ij}^p = \dot{\lambda} \frac{\partial \Phi}{\partial \hat{\sigma}_{ij}} \tag{13}
$$

where $\dot{\lambda} \geq 0$ is the plastic multiplier. The matrix equivalent plastic strain is then related to the plastic power through

$$
p = \int_0^t \dot{p} \, dt = \int_0^t \frac{\hat{\sigma}_{ij} \hat{D}_{ij}^p}{(1-f)\sigma_y} \, dt \tag{14}
$$

where f is the void volume fraction.

The flow stress of the matrix material is described by an extended Voce hardening rule

$$
\sigma_y = \sigma_0 + \sum_{i=1}^{3} Q_i \left(1 - \exp \left(-\frac{\theta_i}{Q_i} p \right) \right) \tag{15}
$$

where σ_0 is the initial yield stress, and Q_i and θ_i are parameters controlling the work hardening. Plastic incompressibility of the matrix material gives the evolution of the void volume fraction as

$$
\dot{f} = (1-f)\hat{D}_{kk}^p \tag{16}
$$

The effective void volume fraction is given by Tvergaard and Needleman (1984)

$$
f^*(f) = \begin{cases} f & \text{if } f \leq f_c \\ f_c + \frac{f_U^* - f_c}{f_F - f_c}(f - f_c) & \text{if } f > f_c \end{cases} \tag{17}
$$

where f_c is the critical void volume fraction where an accelerated void growth is initiated, $f_U^* = 1/q_1$ is the ultimate value, and f_F is the void volume fraction where the material has completely lost its load-carrying capacity. In the subsequent finite element simulations, element deletion is used to describe crack propagation, and the element is deleted when $f = f_F$ in all integration points.

Finally, the loading/unloading conditions of plasticity are given in Kuhn-Tucker form as

$$
\Phi \leq 0, \quad \dot{\lambda} \geq 0, \quad \dot{\lambda} \Phi = 0 \tag{18}
$$

whereas the consistency condition, used to determine the plastic multiplier $\dot{\lambda}$ in the plastic domain, is expressed by

$$
\dot{\lambda} \dot{\Phi} = 0 \tag{19}
$$

The porous plasticity model has been implemented into a user material subroutine (VUMAT) for Abaqus/Explicit (Abaqus, 2014). To ensure sufficient accuracy of the integration point values, sub-stepping is employed (Dæhli et al., 2017).

5.2. Finite element modelling and simulations

In the following, finite element simulations of the tensile tests and the Kahn tear tests for the 6082.25 alloy are presented, which are based on the porous plasticity model described in Section 5.1. The other two alloys demonstrate effects and properties that the porous plasticity model is unable to capture. The 6060 alloy develops a diamond-shaped minimum cross-section in the V-notch tensile tests, see Section 4.3, which can be replicated by crystal plasticity finite element analyses, see Khadyko et al. (2015). Failing to simulate the correct deformation mode will yield uncertainties in the strain measure and thus on the calculated failure strain. For the 6082.50 alloy, the less ductile fracture mode observed especially for loading along TD, see Section 4.3, is poorly described by the porous plasticity model. This model considers growth and
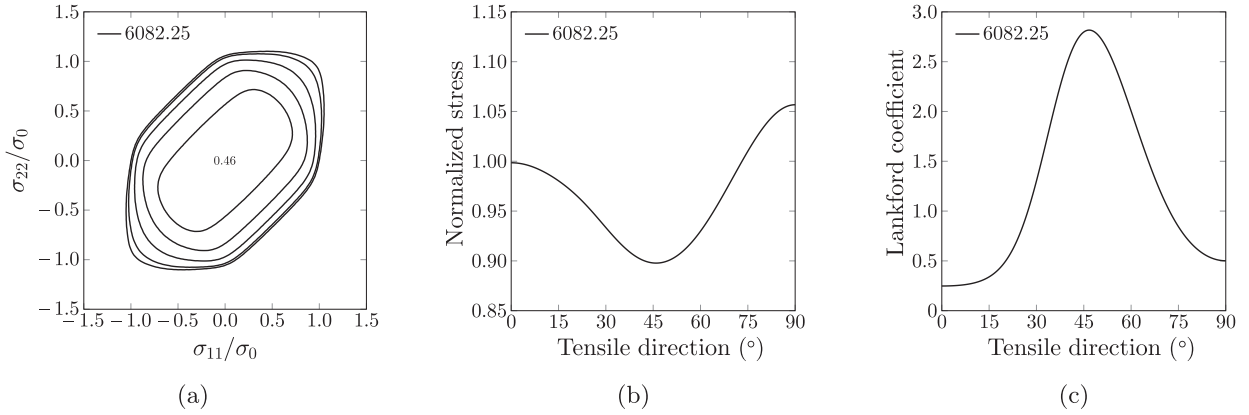
Fig. 14. (a) Initial yield surface of the 6082.25 alloy depicted in the ED-TD plane with contours of normalized shear stress plotted in 0.1 increments, with the maximum value in the centre, and (b) normalized yield stress and (c) Lankford coefficient versus tensile direction with respect to ED for uniaxial tension in the ED-TD plane.

Table 6
Initial yield stress and parameters of the work-hardening rule.

| Material	σ_0 (MPa)	θ_1 (MPa)	Q_1 (MPa)	θ_2 (MPa)	Q_2 (MPa)	θ_3 (MPa)	Q_3 (MPa)
6082.25-AC	99.6	2824.3	78.8	153.1	90.8	–	–
6082.25-WQ	302.1	489.1	30.1	474.5	28.7	50.4	281.8

coalescence of voids in a homogeneous solid which is unable to capture the highly localized damage evolution and failure mode of intercrystalline fracture.

For the ductile 6082.25 alloy, damage evolution and failure is governed by nucleation, growth and coalescence of voids, see Section 4.3, and the porous plasticity model is used to describe both the anisotropic plastic behaviour and the ductile failure process for this material. Isotropic elasticity is assumed in the simulations with a Young's modulus of $E = 70000$ MPa and a Poisson's ratio of $\nu = 0.3$, which are typical values for aluminium. The standard Tvergaard (1981) parameters $q_1 = 1.5$, $q_2 = 1$ are used to define the pressure sensitivity of the yield surface, which were introduced to give better agreement with unit cell analyses. As an alternative, these parameters could have been determined from unit cell computations (see, e.g., Dæhli et al., 2017) and may depend on, e.g., the work-hardening behaviour and plastic anisotropy of the material. Thus, the remaining model parameters to identify are the anisotropy parameters controlling the shape of the yield surface ($\hat{c}_{ij}^{(1)}$, $\hat{c}_{ij}^{(2)}$, a), the work-hardening parameters (σ_0, Q_i, θ_i; $i = 1, 2, 3$), and the porous plasticity damage parameters (f_0, f_c, f_F).

The anisotropy parameters controlling the shape of the yield surface concerning deviatoric stress states can be identified either from a large number of experimental tests (Fourmeau, Børvik, Benallal, Lademo, & Hopperstad, 2011) or from micromechanical simulations (Frodal, Dæhli, Børvik, & Hopperstad, 2019) by combining crystal plasticity with the finite element method (CP-FEM). The anisotropic yield surfaces of these alloys have previously been calibrated by Frodal et al. (2019) utilising CP-FEM. Fig. 14 depicts the initial yield surface of the 6082.25 alloy for porosity $f = 0$, together with the normalized initial yield stress in uniaxial tension, and Lankford coefficients versus tensile direction in the ED-TD plane.

The finite element meshes of the smooth and V-notch tensile specimens and Kahn tear test specimen are shown in Fig. 15. Due to the orthotropic material symmetry, only one-eighth of the smooth and V-notch tensile specimens and one-quarter of the Kahn tear test specimen are modelled to reduce the computational time. Linear eight-node solid elements with reduced integration (C3D8R) are used. The dimensions of the elements located in the centre of the specimens are $30 \times 40 \times 40$ μm³, with the shortest element length along the tensile direction. Mass scaling is used to reduce the computational time, and it is ensured that the response is quasi-static, i.e., that the kinetic energy is negligible compared with the internal energy. The appropriate symmetry boundary conditions are enforced and loading is applied to the end of the smooth and V-notch tensile specimens. An analytic rigid pin is used to apply the load onto the Kahn tear test specimen, where a friction-less surface-to-surface contact formulation is used between the specimen and the rigid pin.

In order to determine the work-hardening parameters of the materials, finite element simulations of the tensile test on the smooth specimen are run in Abaqus/Explicit combined with the non-linear optimization software LS-OPT (Stander et al., 2015). The parameters of Eq. (15) are calibrated by minimising the mean squared error between the stress-strain curves up to failure from the finite element simulation and the experimental tests. During this calibration, the material is assumed to have zero porosity (i.e., $f = 0$). The work-hardening parameters of the water-quenched material have previously been determined, and the reader is referred to Frodal et al. (2019) for further details on the calibration process. Table 6 presents the resulting initial yield stress and the work-hardening parameters, where the parameter set has been adjusted to account for the minor softening introduced by the initial porosity calibrated below (i.e., $f = f_0$).
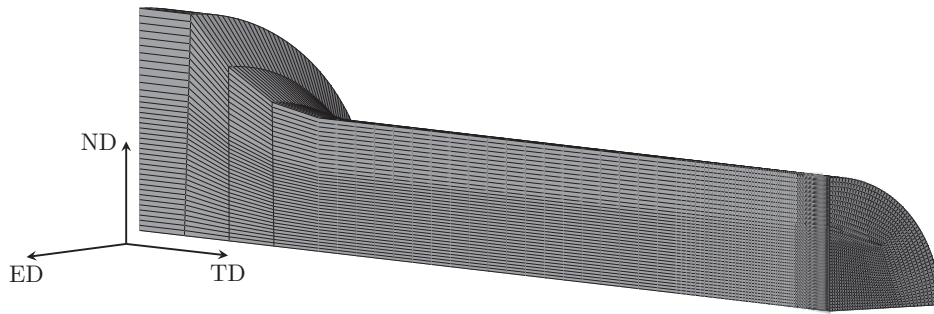
(a)
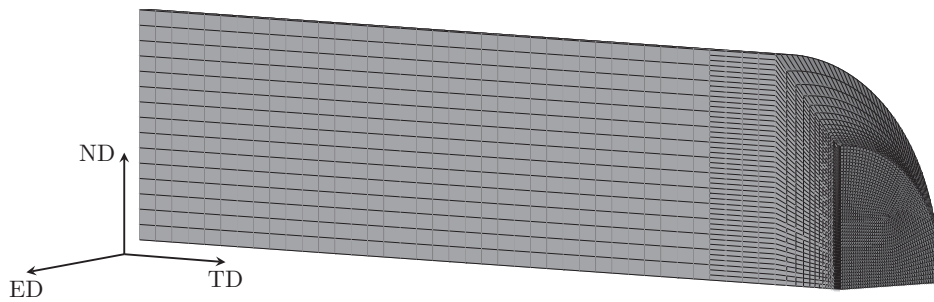
(b)
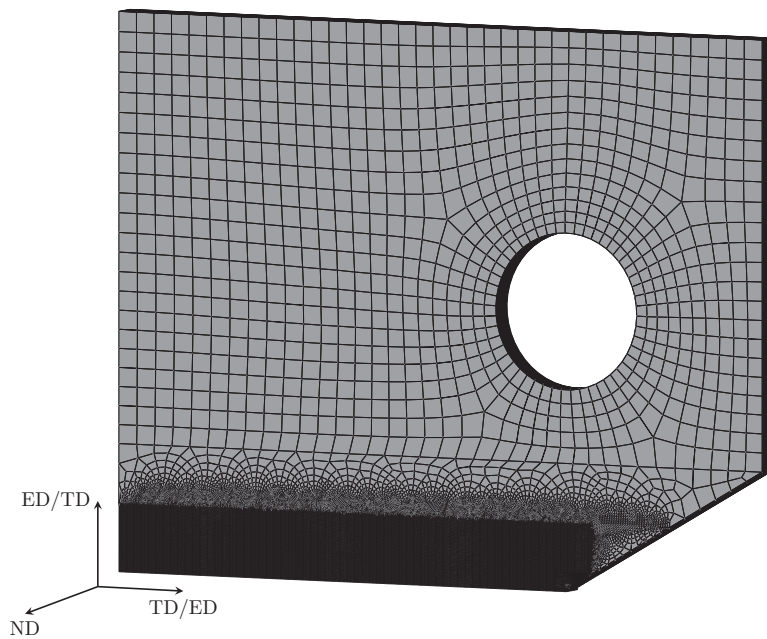
(c)

Fig. 15. Finite element meshes of (a) the smooth tensile specimen, (b) the V-notch tensile specimen, and (c) the Kahn tear test specimen.

Table 7
Porous plasticity parameters, including initial porosity f_0, critical porosity f_c, and porosity at complete material failure f_F.

Material	f_0	f_c	f_F
6082.25-AC	$1.20 \cdot 10^{-3}$	$8.39 \cdot 10^{-3}$	$2.12 \cdot 10^{-1}$
6082.25-WQ	$1.30 \cdot 10^{-3}$	$8.38 \cdot 10^{-3}$	$6.08 \cdot 10^{-2}$

The damage parameters of the porous plasticity model, including the initial porosity f_0, the critical porosity f_c, and the porosity at complete material failure f_F, are here calibrated using a similar approach as with the initial yield strength and the work-hardening parameters. Simulations of tensile tests on the smooth and V-notch specimens are performed in Abaqus/Explicit, and the distance between the point of maximum true stress (i.e., the true stress at incipient strain softening) is minimized simultaneously for both tests by means of the LS-OPT software. This ensures that the point of failure is precisely captured for both the tensile tests on the smooth and V-notch specimens. The resulting porous plasticity parameters are given in Table 7.

The stress-strain curves from the finite element simulations of the tensile tests of the smooth and V-notch specimens are shown in Figs. 7 and 8, respectively. A good agreement is found between the numerical and experimental results up to fracture for both the smooth and V-notch specimens, and the point of maximum true stress is well captured. In the tests of the smooth tensile specimens, the stress level drops abruptly after reaching the point of maximum true stress. Similarly, the stress level drops rapidly for the water-quenched material in the finite element simulation, whereas the decrease is less swift in the simulation of the air-cooled material. In the tests of the V-notch tensile specimens, accelerated damage induced softening is observed and the stress level decreases after the point of maximum true stress before a sudden drop of the stress level occurs. The same trends are seen in the numerical simulations, but the sudden drop in stress level is somewhat delayed. Thus, more energy is dissipated in the simulations than in the experiments before the material has lost all of its load-carrying capacity, i.e., the tensile ductility is somewhat overestimated in the simulations. It should however be noted that predictions of crack propagation by element deletion are mesh dependent and more accurate results might possibly have been obtained with an even finer mesh.

The resulting force-displacement curves from the simulations of the Kahn tear tests are presented in Fig. 9. The peak force is slightly underestimated in the simulations for both the water-quenched and air-cooled materials, and the drop in the load level is not as steep after the peak force as observed in the experiments. In view of the results obtained in the simulations of the V-notch specimen subjected to tensile loading, it is reasonable to attribute the lower slope of the numerical force-displacement curves and the higher energy dissipation during crack propagation to the more ductile failure mode of the finite element model. In addition, errors in the calibrated yield surface may become apparent for this loading condition. However, the differences observed experimentally between the water-quenched and air-cooled materials are well captured in the simulations, i.e., the predicted load level for the water-quenched material drops below that of the air-cooled material when the displacement increases.

Fig. 16 depicts contours of the von Mises equivalent strain at failure initiation and during crack propagation in the Kahn tear tests from the experiment and the finite element simulation of the air-cooled 6082.25 alloy loaded along ED. In the experiment, the strain field was calculated based on full-field measurements of the surface displacement field using digital image correlation (DIC). The strain fields from the experiment and the simulation are in relatively good agreement. Highly localized deformation is observed close to the notch and crack tip, where the equivalent strain is the highest. At peak force ①, "butterfly wing" shaped contours are seen close to the notch and further away from the notch tip the contours are more circular. As the crack progresses through the alloy, ②-⑥, the "butterfly wing" shaped contours persist in front of the crack tip. Fig. 17 depicts the corresponding image locations on the force-displacement curve for the air-cooled 6082.25 alloy loaded along ED.

Albeit, a large set of parameters is used in the porous plasticity model to describe the plastic anisotropy of the materials, only 3 damage parameters, f_0, f_c and f_F, are included. Thus, the finite element results indicate that a good description of the plastic deformation and the stress states occurring prior to final failure is critical for ductile fracture. It should also be noted that all model parameters were calibrated based solely on crystallographic texture measurements combined with crystal plasticity finite element simulations, and two mechanical tests subjecting the material to different stress states.

6. Discussion

From the microstructural investigation in Section 4.1, it is evident that the precipitate structure is markedly influenced by the quench rate. A slower quench rate, i.e., air-cooling, gives a reduced volume fraction of strengthening precipitates within the grains, and wider PFZs at the grain boundaries and around the dispersoids. The influence of quench rate on the number density, cross-sectional area and length of the precipitates depends on the alloy. The lean 6060 alloy has a lower number density of precipitates after air-cooling and the precipitates have a larger cross-section area and length. The air-cooling is detrimental to the precipitate structure of the 6082.25 alloy, which has a fibrous grain structure with flat, elongated grains and small sub-grains, and results in an inhomogeneous microstructure where entire grains are free of strengthening
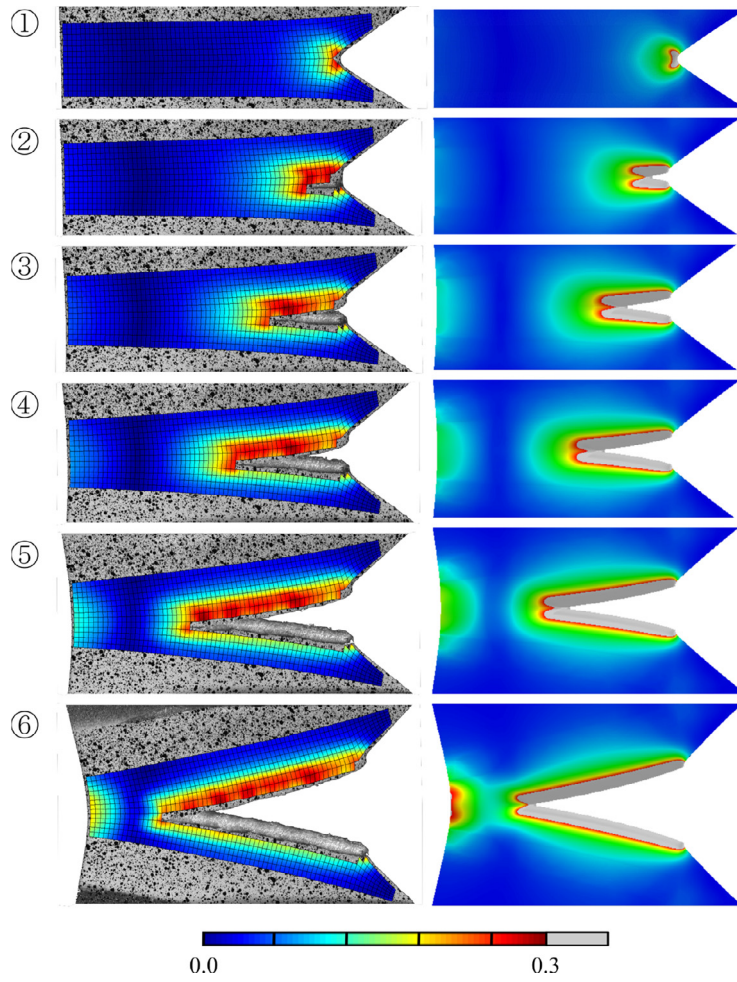
Fig. 16. Contour plot of von Mises equivalent strain during crack propagation in the Kahn tear test of the air-cooled 6082.25 alloy loaded along ED: (left) experiment and (right) finite element analysis. Extracted images from the experiment and finite element analyses at the same crack opening displacement, see Fig. 17.
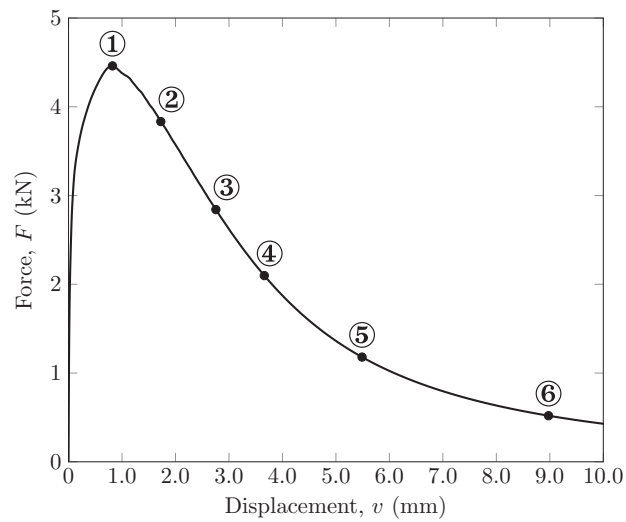

Fig. 17. Force-displacement curve from the finite element analysis of the Kahn tear test with the air-cooled 6082.25 alloy loaded along ED. Markers correspond to the images in Fig. 16.
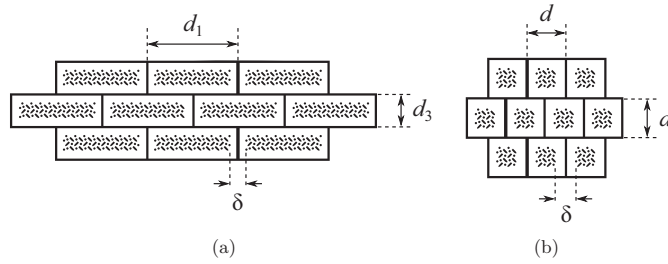
Fig. 18. Schematic diagram showing the assumed PFZs in the different materials. The hatched regions illustrate precipitates that form within the matrix material after ageing, while the white regions are PFZs: (a) elongated grains, and (b) equiaxed grains.

precipitates. Precipitation in the 6082.50 alloy also becomes inhomogeneous after air-cooling, consisting of strong regions with dense precipitation resembling the water-quenched state and relatively large soft regions around dispersoids (due to PFZs around dispersoids).

The reduced number density of precipitates in the air-cooled 6060 alloy is most likely due to diffusion of solute and vacancies to GBs and other inhomogeneities in the microstructure. In the 6082.25 alloy, the inhomogeneous precipitation observed is due to overlapping PFZs from GBs and dispersoids. PFZs around dispersoids are also the reason for the inhomogeneous precipitate microstructure observed in the 6082.50 alloy. The physical origin of the increased precipitation outside these PFZs compared to the water-quenched state of this alloy has not been established. This particular aspect is outside of the scope of the current article, but should be of interest for future studies.

Albeit the width of the PFZs increases if air-cooling is used instead of water-quenching in all the three alloys, the relative increase depends on the alloy and is largest for the high-strength 6082 alloys. The reason for this observation is the very narrow PFZs in these alloys after water-quenching due to the increased precipitation potential of high-solute alloys. If one considers the absolute change in PFZ widths instead, the PFZs in the 6060 alloy widen more than those in the 6082.50 alloy. However, it should be mentioned here that there are some challenges in measuring PFZ widths in the dense alloys. In the 6082.25 alloy, precipitates were rarely observed, and in the 6082.50 alloy, few grain boundaries could be found in the TEM specimens due to the large grains.

In the following, the physically based model NaMo is used to predict the effect of different cooling conditions, grain structures and PFZ widths on the resulting yield strength after the final ageing heat treatment. NaMo is a combined precipitation, yield strength and work hardening model for 6xxx alloys. The model predicts the evolution of the precipitate structure for each time step during a non-isothermal heat treatment based on user-defined inputs including the alloy composition. The relevant parameters from the precipitate module of NaMo are used to calculate the yield stress and the work hardening rate through dislocation mechanics, and a complete stress-strain curve at room temperature can be predicted. The model has previously been outlined in several publications, see, e.g., Myhr, Grong, and Andersen (2001), Myhr, Grong, and Pedersen (2010), Myhr, Grong, and Schäfer (2015), Granum, Myhr, Børvik, and Hopperstad (2018), and the readers are referred to these for a comprehensive description of the underlying theory and mathematical framework of NaMo. In the present article, only some special characteristics of the model, which are related to quench sensitivity, are described in more details, to explain how the model handles the different grain structures and PFZ widths for the alloys in the present investigation.

The model assumes that the alloy consists of two different materials, i.e., PFZ material that forms adjacent to grain boundaries and dispersoids, and matrix material that forms outside the PFZs. NaMo estimates the yield stress in each of these zones as well as the overall volume fraction of PFZs in the alloy based on grain structure data, dispersoid density data and PFZ widths. In the present study, the dispersoid density data of the two 6082 alloys has been determined using the Alstruc model (Dons, 2001; Dons, Jensen, Langsrud, Trømborg, & Brusethaug, 1999). The estimated dispersoid number densities are $4.6 \cdot 10^{19}$ #/m^3 and $1.0 \cdot 10^{19}$ #/m^3, and the average dispersoid diameters are 54 nm and 84 nm for the 6082.25 and 6082.50 alloy, respectively.

Fig. 18 shows how the volume fraction of PFZs is estimated for the different materials in the present work. For large elongated recrystallized grains, like the ones in the 6082.50 alloy, the grain structure is illustrated in Fig. 18a, where d_1 and d_3 are average grain sizes along the extrusion direction (ED) and thickness direction (ND), respectively. The grain size d_2 in the transverse direction (TD) is not shown in the two-dimensional figure, but for the 6082.50 alloy, it is about the same size as d_1. The volume fraction of PFZ, i.e., f_{PFZ}, for this type of grain structure can be estimated as follows

$$f_{PFZ} = 1 - \frac{(d_1 - \delta)(d_2 - \delta)(d_3 - \delta)}{d_1 d_2 d_3} \tag{20}$$

Here, δ is the total PFZ width, i.e. on both sides of the grain boundary, and it is assumed that δ is the same in all the three directions ED, TD, and ND. The recrystallized grains in the 6060 alloy are assumed to be equiaxed like the one schematically illustrated in Fig. 18b. In this case, f_{PFZ} can be calculated by substituting d_1, d_2 and d_3 in Eq. (20) by an average grain size

Table 8
Calculated volume fractions of PFZs from grains, subgrains, and the total volume fraction, in addition to calculated yield stresses, where σ_M, σ_{PFZ} and σ_0 are the yield stress of the matrix material, the PFZ material and the overall yield stress, respectively.

Material	f_{PFZ} (%)			σ_M (MPa)	σ_{PFZ} (MPa)	σ_0 (MPa)
	grains	subgrains	total			
6060-AC	2.2	–	2.2	166	90	164
6060-WQ	0.7	–	0.7	191	42	190
6082.25-AC	3.6	42.0	45.6	187	129	161
6082.25-WQ	0.7	8.9	9.6	327	132	308
6082.50-AC	< 0.1	–	< 0.1	164	107	164
6082.50-WQ	< 0.1	–	< 0.1	348	129	348

d, which gives

$$f_{PFZ} = 1 - \frac{(d - \delta)^3}{d^3} \tag{21}$$

Eq. (21) is not restricted to recrystallized grains, but can also be used to estimate the volume fraction of PFZs associated with the equiaxed subgrain structure of the 6082.25 alloy based on the measured average subgrain-size.

NaMo also calculates the volume fraction of PFZ associated with dispersoids by assuming that each particle is encircled by a spherical PFZ. The volume fraction is then simply given as the volume of PFZ for each particle multiplied by the particle number density N_v so that

$$f_{PFZ} = \frac{4}{3}\pi \left[(r + \Delta r)^3 - r^3 \right] N_v \tag{22}$$

Here r and Δr are the radius of the particle and the width of the PFZ adjacent to the particle surface, respectively. Note that in the following calculations, the contribution from PFZs around dispersoids is neglected as the PFZ width around these particles has not been determined in the present work.

In the estimation of the yield stress of the PFZ regions, it is simply assumed that this material does not respond to any ageing. This means that there is no nucleation of particles in these zones. The yield stress is therefore given by the solid so-lution concentrations of the different elements after the water-quenching or air-cooling described in Fig. 1, as calculated by NaMo. For the matrix material, NaMo calculates the precipitation and resulting yield stress during the subsequent artificial ageing without any modifications of the model. In both the PFZ and matrix material, NaMo accounts for the negative effect of the dispersoids on the resulting yield strength due to coarse β'-type of particles that may nucleate at dispersoids during cooling (Myhr, Engler, Leinum, Brinkman, & Furu, 2017). In the PFZ material, this lowers the solid solution strengthening due to the consumption of Mg and Si in the formation of these non-hardening particles during the cooling stage. In the matrix material, this reduction in Mg and Si lowers the hardening potential of the alloy, which in turn leads to a reduction in yield stress after artificial aging (Myhr et al., 2017).

Finally, when the volume fraction of PFZs and the yield stress in each of the two zones, i.e., matrix and PFZ, are known, the resulting yield stress σ_0 is simply calculated as follows

$$\sigma_0 = (1 - f_{PFZ})\sigma_M + f_{PFZ} \cdot \sigma_{PFZ} \tag{23}$$

Here, σ_M and σ_{PFZ} are the yield stress of the matrix material and the PFZ material, respectively. Eq. (23) is obviously a crude approximation of the integrated effect of the two individual materials on the resulting yield stress. In reality, σ_0 depends not only on the individual volume fractions of PFZ material and matrix material, but also on the spatial distribution and size of the individual PFZs.

Table 8 shows the calculated volume fractions of PFZs for the six different combinations of alloy and cooling rate, and the corresponding yield stresses of the matrix material, the PFZ material, and the overall yield stress. Fig. 19 shows a comparison between the calculated yield stresses σ_0 from Table 8, and the corresponding measured values given in Table 3. It is evident that the agreement between simulation results and measurements is good, and NaMo seems to capture the effect of alloy composition, grain structure, PFZ widths and cooling rate on the resulting yield stress with a good degree of accuracy.

The predictions of yield stress from NaMo are very close to the experimental values for all the alloys and heat treatments. In the 6060 alloy, NaMo predicts an overall reduction in precipitate strengthening upon air-cooling, and the effect of PFZs is low. In the 6082.25 alloy, the dramatic increase in PFZ volume fraction is responsible for the much lower yield stress of the air-cooled alloy compared to the water-quenched alloy. For the 6082.50 alloy, NaMo predictions are also good. In this case, NaMo predicts an overall lower number density of precipitates in the air-cooled alloy compared to the water-quenched alloy, which is responsible for the reduction in yield stress, as the volume fraction of PFZs are estimated to be relatively low. The TEM investigations indicated, however, that σ_M should be relatively similar for the air-cooled and water-quenched states of this alloy, and that the inhomogeneous precipitate microstructure observed after air-cooling should increase the volume fraction of PFZs. It appears that the complex precipitation behaviour of this alloy is not captured by NaMo, and
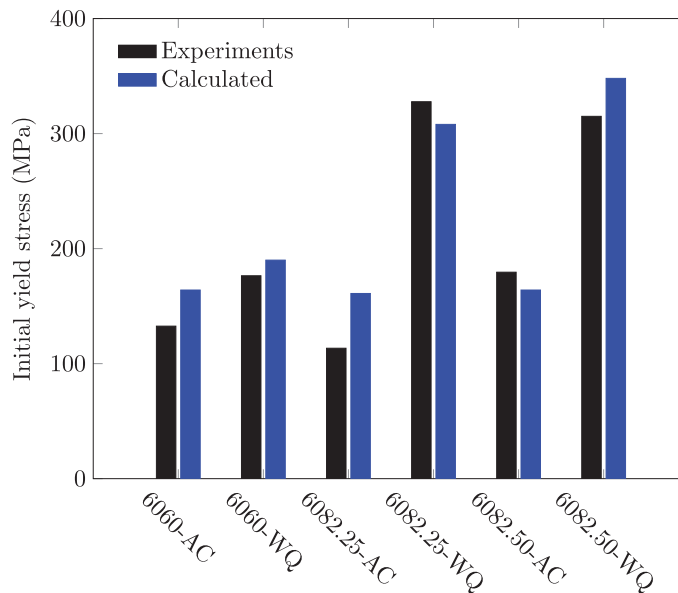
Fig. 19. Comparison between the measured (Table 3) and calculated (Table 8) yield stress for the different alloys and cooling conditions.

that the inhomogeneous distribution of precipitates and PFZs around dispersoids leads to a state of complex yielding and plastic flow in the material. This complex microstructure will probably affect the response observed in the tensile tests, and may explain the greater work-hardening rate in the air-cooled state compared to the water-quenched state of the 6082.50 alloy. Because the precipitation in these two materials primarily differs with respect to PFZs around dispersoids, making the air-cooled microstructure quite inhomogeneous, the difference in work hardening may be related to storage of dislocations within soft PFZs around hard impenetrable particles. Kawabata and Izumi (1976) showed that the initial yield stress and plastic deformation of materials can depend on the PFZs, and of the strength difference between precipitate strengthened regions and PFZs. In particular, they suggested that early strain localization can lead to a high initial work-hardening rate and that this effect can increase with increasing PFZ size. This is in agreement with our experimental findings, where a higher work-hardening rate is observed for the air-cooled materials.

In previous studies on various aluminium alloys, the tensile ductility has been found to decrease with increasing yield strength for similar grain structure (Hannard et al., 2016; Lloyd, 2003; Pedersen, Westermann, Furu, Børvik, & Hopperstad, 2015; Westermann, Pedersen, Furu, Børvik, & Hopperstad, 2014). Consistent findings are made in this study, i.e., the tensile tests on air-cooled smooth and V-notch specimens give higher failure strain than those on water-quenched specimens. A plausible explanation for this finding is that the higher yield strength of the water-quenched materials accelerates void nucleation at constituent particles (Pineau et al., 2016). In addition, the work-hardening rate is greater for the air-cooled than for the water-quenched materials, see Fig. 7 and Table 6, which is typically observed when the yield strength is reduced. The higher work-hardening rate of the air-cooled materials contributes to distributing the plastic deformation over a larger area of the specimen which delays necking, plastic localization and ductile fracture (Frodal, Morin, Børvik, & Hopperstad, 2020).

The crack initiation energies (UIEs) for the 6060 and 6082.25 alloys are similar for the air-cooled and water-quenched materials, see Table 5. As the peak force of the Kahn tear tests is lower after air-cooling, see Fig. 9, the displacement to fracture initiation is larger than after water-quenching. This is consistent with the observed higher tensile ductility after air-cooling from the smooth and V-notch specimens. In contrast, air-cooling gives a slightly reduced crack initiation energy for the 6082.50 alloy compared to water-quenching.

The crack propagation energies (UPEs) are significantly affected by the quench rate for all the three alloys. For the 6060 alloy, the energy required for crack propagation is lower for air-cooling, but the difference in UPE compared with water-quenching is of the same magnitude as the difference in UPE between loading along ED and TD. Thus, the effect of quench rate on the UPE is equally large as the effect of plastic anisotropy for this alloy. Albeit a significant amount of intercrystalline fracture is observed for loading along TD, see Fig. 11, the UPE is higher than what was observed for loading along ED, where very little intercrystalline fracture was observed. This indicates that the plastic anisotropy, caused by the crystallographic texture, has a significant influence on the UPE for this alloy having equiaxed grains. While the UPE is reduced after air-cooling for the 6060 alloy, it is drastically increased after air-cooling for the 6082.25 alloy compared with water-quenching. This suggests that the microstructure of this alloy after air-cooling, comprised of precipitate-free regions spanning entire grains, is favourable for the tear resistance compared to the water-quenched condition where the material consists of hard precipitate-strengthened grains surrounded by thin PFZs. For the 6082.50 alloy, the UPE is lower for the air-cooled ma-

terial when loaded along ED and markedly higher when loaded along TD compared with the water-quenched material. These findings can be linked to the amount of intercrystalline fracture observed on the fracture surfaces, see Fig. 13, as the intercrystalline fracture reduces the UPE (Dumont et al., 2003, 2004a, 2004b; Morgeneyer et al., 2008). When the water-quenched material is suseptible to intercrystalline fracture, as the 6082.50 alloy is when loaded in TD, air-cooling increases the UPE by decreasing the amount of intercrystalline fracture. This is likely due to the increased capacity of wider PFZs to alleviate stresses ahead of slip bands, as suggested by Ryum (1968) and Kawabata and Izumi (1976). However, when the water-quenched material is not susceptible to intercrystalline fracture, i.e., when the 6082.50 alloy is loaded in ED, air-cooling reduces the UPE despite a lower yield stress, by promoting intercrystalline fracture instead. In this case, the increased amount of intercrystalline fracture may be related to strain localization and preferential deformation in the wider PFZs, or the increased number of large particles (precipitates on dispersoids) that may act as void nucleation sites (Vasudévan & Doherty, 1987).

The porous plasticity model is capable of describing the plastic flow and failure initiation in the tensile tests on smooth and V-notch specimens with good accuracy, while the crack propagation speed is underestimated, i.e., the stress level in the simulations drops more gradually than in the experiments. The failure initiation is well predicted also for the Kahn tear test specimen, although the peak force is slightly underestimated, most probably due to inaccuracies in the calibrated yield surface. During crack propagation, the predicted force level is higher than that observed experimentally and the dissipated energy due to plastic deformation is overestimated. In the numerical simulations, the crack propagation is predicted by element deletion, and as such the crack tip radius is governed by the element size, rendering the crack propagation highly mesh dependent. As a result, the adopted failure modelling approach, i.e., combining porous plasticity with element erosion, is best suited for situations where the mechanisms of damage evolution and fracture are not as localized as in the Kahn tear test. However, it is assumed that the results could be improved by further decreasing the mesh size and thus increase the crack propagation speed in the simulations, see e.g. Besson (2010) for a detailed discussion of mesh size sensitivity in finite element simulation of ductile fracture.

7. Concluding remarks

The role of quench rate after the solution heat-treatment on the plastic flow and fracture of three aluminium alloys was studied by conducting tensile tests on smooth and V-notched specimens as well as Kahn tear tests. The three AlMgSi alloys considered, i.e., 6060, 6082.25 and 6082.50, had different grain structure, grain size and crystallographic texture. The alloys were differently affected by the quench rate, as obtained by water-quenching or air-cooling. The TEM study showed that air-cooling is detrimental for precipitation in all alloys. In lean alloys, like the 6060 alloy, the detrimental effect is due to an overall reduction in precipitate number density and slightly coarser precipitates. In dense alloys that contain dispersoids, like the 6082 alloys, PFZs around the dispersoids become much wider after air-cooling. If the density of dispersoids is high and the grain size is small, such as in the 6082.25 alloy, the PFZs of adjacent dispersoids overlap, and due to the small grain and subgrain size in this material, entire grains can become free of precipitates. If the density of dispersoids is low and the grain size is relatively large, as in the 6082.50 alloy, PFZs around dispersoids do not necessarily overlap, resulting in an inhomogenous microstructure consisting of strong regions of dense preciptiation a certain distance from dispersoids that are surrounded by wide PFZs. Air-cooling gave consistently larger precipitate free zones around both GBs and dispersoids in the three alloys than water-quenching.

The changes in the precipitatate microstructure affect the initial yield stress, and air-cooling gave a lower yield stress for all three alloys. These changes were captured by the nanostructure model NaMo with good accuracy. In all materials, NaMo was able to predict correct precipitation and strengthening contributions, except for the air-cooled 6082.50 alloy where a homogeneous and reduced precipitation was predicted. In this material, the microstructure is highly complex and inhomogeneous, which is not easily captured by such models. The plastic behaviour of this material is possibly linked to a complex interplay between the soft PFZs and hard precipitate strengthened regions. Enhancing the predictive capabilities of NaMo and investigating this complex interplay are tasks left for further work.

In the Kahn tear tests, the displacement to crack initiation was larger for the air-cooled materials, as the crack initiation energies were similar for different quench rates, but the peak force was drastically reduced. The crack propagation energy was markedly affected by the quench rate after the solution heat-treatment, but the effect was different for the different alloys. Compared with water-quenching, air-cooling led to lower crack propagation energy for the 6060 alloy and higher crack propagation energy for the 6082.25 alloy, where entire grains are free of strengthening precipitates due to the slow cooling. For the 6082.50 alloy, the influence of quench rate on the crack propagation energy was different for the two loading directions, i.e., either along the extrusion direction or along the transverse in-plane direction, and can be linked to the amount of intercrystalline fracture observed on the fracture surface, as intercrystalline fracture reduces the crack propagation energy.

The anisotropic porous plasticity model used in the finite element simulations was able to precisely capture the fracture initiation in all the specimen geometries for the 6082.25 alloy. Albeit the dissipated energy due to plastic deformation was overestimated during crack propagation, the overall response was well captured, and the porous plasticity model was able to account for the influence of quench rate. The 6060 and 6082.50 alloys demonstrated effects and properties that the porous plasticity model was unable to describe. Thus, there is a need for more advanced physically-based models which are

able to account for both the complex anisotropy of textured aluminium alloys and intercrystalline fracture due to the grain boundary PFZs in these materials.

Declaration of Competing Interest

The authors declare no competing interests.

Acknowledgments

References

Abaqus Version 6.14. (2014). *Dassault Systemès Simulia Corporation Providence*. Rhode Island, USA.
Andersen, S. J. (1995). Quantification of the Mg2Si β" and β' phases in AlMgSi alloys by transmission electron microscopy. *Metallurgical and Materials Transactions A, 26*(8), 1931–1937.
ASTM (2001). ASTM B871-01 standard test method for tear testing of aluminum alloy products. 10.1520/B0871-01.
Barlat, F., Aretz, H., Yoon, J., Karabin, M., Brem, J., & Dick, R. (2005). Linear transfomation-based anisotropic yield functions. *International Journal of Plasticity, 21*(5), 1009–1039.
Besson, J. (2010). Continuum models of ductile fracture: A review. *International Journal of Damage Mechanics, 19*(1), 3–52.
van den Boogaard, T., Havinga, J., Belin, A., & Barlat, F. (2016). Parameter reduction for the Yld2004-18p yield criterion. *International Journal of Material Forming, 9*(2), 175–178.
Chen, Y., Pedersen, K. O., Clausen, A. H., & Hopperstad, O. S. (2009). An experimental study on the dynamic fracture of extruded AA6xxx and AA7xxx aluminium alloys. Materials Science and Engineering: A, *523*(1–2), 253–262.
Christiansen, E., Marioara, C. D., Marthinsen, K., Hopperstad, O. S., & Holmestad, R. (2018). Lattice rotations in precipitate free zones in an Al-Mg-Si alloy. *Materials Characterization, 144*, 522–531.
Conserva, M., & Fiorini, P. (1973). Interpretation of quench-sensitivity in Al-Zn-Mg-Cu Alloys. *Metallurgical Transactions, 4*(3), 857–862.
De Haas, M., & De Hosson, J. T. M. (2002). On the effects of thermomechanical processing on failure mode in precipitation-hardened aluminium alloys. *Journal of Materials Science, 37*(23), 5065–5073.
Deschamps, A., Texier, G., Ringeval, S., & Delfaut-Durut, L. (2009). Influence of cooling rate on the precipitation microstructure in a medium strength Al-Zn-Mg alloy. *Materials Science and Engineering: A, 501*(1), 133–139.
Dons, A. L. (2001). The alstruc homogenization model for industrial aluminum alloys. *Journal of Light Metals, 1*(2), 133–149.
Dons, A. L., Jensen, E. K., Langsrud, Y., Trømborg, E., & Brusethaug, S. (1999). The alstruc microstructure solidification model for industrial aluminum alloys. *Metallurgical and Materials Transactions A, 30*(8), 2135–2146.
Dons, A. L., & Lohne, O. (1983). Quench sensitivity of AlMgSi-alloys containing Mn or Cr. *MRS Proceedings, 21*, 723.
Dowling, J. M., & Martin, J. W. (1976). The influence of MN additions on the deformation behaviour of an Al-Mg-Si alloy. *Acta Metallurgica, 24*(12), 1147–1153.
Dumont, D., Deschamps, A., & Brechet, Y. (2003). On the relationship between microstructure, strength and toughness in AA7050 aluminum alloy. *Materials Science and Engineering: A, 356*(1), 326–336.
Dumont, D., Deschamps, A., & Brechet, Y. (2004a). A model for predicting fracture mode and toughness in 7000 series aluminium alloys. *Acta Materialia, 52*(9), 2529–2540.
Dumont, D., Deschamps, A., Bréchet, Y., Sigli, C., & Ehrström, J. C. (2004b). Characterisation of precipitation microstructures in aluminium alloys 7040 and 7050 and their relationship to mechanical behaviour. *Materials Science and Technology, 20*(5), 567–576.
Dæhli, L. E. B., Faleskog, J., Børvik, T., & Hopperstad, O. S. (2017). Unit cell simulations and porous plasticity modelling for strongly anisotropic FCC metals. *European Journal of Mechanics - A/Solids, 65*, 360–383.
Evancho, J. W., & Staley, J. T. (1974). Kinetics of precipitation in aluminum alloys during continuous cooling. *Metallurgical Transactions, 5*(1), 43.
Falahati, A., Lang, P., & Kozeschnik, E. (2012). Precipitation in Al-alloy 6016 - the role of excess vacancies. *Materials Science Forum, 706*, 317–322. Trans Tech Publications.
Fourmeau, M., Børvik, T., Benallal, A., Lademo, O. G., & Hopperstad, O. S. (2011). On the plastic anisotropy of an aluminium alloy and its influence on constrained multiaxial flow. *International Journal of Plasticity, 27*(12), 2005–2025.
Frodal, B. H., Dæhli, L. E. B., Børvik, T., & Hopperstad, O. S. (2019). Modelling and simulation of ductile failure in textured aluminium alloys subjected to compression-tension loading. *International Journal of Plasticity, 118*, 36–69.
Frodal, B. H., Morin, D., Børvik, T., & Hopperstad, O. S. (2020). On the effect of plastic anisotropy, strength and work hardening on the tensile ductility of aluminium alloys. *International Journal of Solids and Structures, 188–189*, 118–132.
Frodal, B. H., Pedersen, K. O., Børvik, T., & Hopperstad, O. S. (2017). Influence of pre-compression on the ductility of AA6xxx aluminium alloys. *International Journal of Fracture, 206*(2), 131–149.
Granum, H., Myhr, O. R., Børvik, T., & Hopperstad, O. S. (2018). Nanostructure-based finite element analyses of aluminium profiles subjected to quasi-static axial crushing. *Thin-Walled Structures, 131*, 769–781.
Gurson, A. L. (1977). Continuum theory of ductile rupture by void nucleation and growth: Part I—Yield criteria and flow rules for porous ductile media. *Journal of Engineering Materials and Technology, 99*(1), 2–15.
Hannard, F., Pardoen, T., Maire, E., Bourlot, C. L., Mokso, R., & Simar, A. (2016). Characterization and micromechanical modelling of microstructural hetero-geneity effects on ductile fracture of 6xxx aluminium alloys. *Acta Materialia, 103*, 558–572.
Kawabata, T., & Izumi, O. (1976). Ductile fracture in the interior of precipitate free zone in an Al-6.0%Zn-2.6%Mg alloy. *Acta Metallurgica, 24*(9), 817–825.
Khadyko, M., Dumoulin, S., Børvik, T., & Hopperstad, O. S. (2014). An experimental-numerical method to determine the work-hardening of anisotropic ductile materials at large strains. *International Journal of Mechanical Sciences, 88*, 25–36.
Khadyko, M., Dumoulin, S., Børvik, T., & Hopperstad, O. S. (2015). Simulation of large-strain behaviour of aluminium alloy under tensile loading using anisotropic plasticity models. *Computers & Structures, 157*, 60–75.
Khadyko, M., Marioara, C. D., Ringdalen, I. G., Dumoulin, S., & Hopperstad, O. S. (2016). Deformation and strain localization in polycrystals with plastically heterogeneous grains. *International Journal of Plasticity, 86*, 128–150.
Lloyd, D. J. (2003). The scaling of the tensile ductile fracture strain with yield strength in Al alloys. *Scripta Materialia, 48*(4), 341–344.
Lohne, O., & Naess, O. J. (1979). The effect of dispersoids and grain size on mechanical properties of AlMgSi alloys. In P. Haasen, V. Gerold, & G. Kostorz (Eds.), *Strength of metals and alloys* (pp. 781–788). Pergamon.
Maire, E., Zhou, S., Adrien, J., & Dimichiel, M. (2011). Damage quantification in aluminium alloys using in situ tensile tests in X-ray tomography. *Engineering Fracture Mechanics, 78*(15), 2679–2690.
Marioara, C. D., Andersen, S. J., Zandbergen, H. W., & Holmestad, R. (2005). The influence of alloy composition on precipitates of the Al-Mg-Si system. *Metallurgical and Materials Transactions A, 36*(13), 691–702.

Milkereit, B., Schick, C., & Kessler, O. (2010). Continuous cooling precipitation diagrams depending on the composition of aluminum-magnesium-silicon alloys. In *Proceedings of the 12th international conference on aluminium alloys, yokohama, japan* (pp. 407–412).

Milkereit, B., & Starink, M. J. (2015). Quench sensitivity of Al-Mg-Si alloys: A model for linear cooling and strengthening. *Materials & Design, 76*, 117–129.

Morgeneyer, T. F., Starink, M. J., Wang, S. C., & Sinclair, I. (2008). Quench sensitivity of toughness in an Al alloy: Direct observation and analysis of failure initiation at the precipitate-free zone. *Acta Materialia, 56*(12), 2872–2884.

Myhr, O. R., Engler, O., Leinum, J. R., Brinkman, H. J., & Furu, T. (2017). Modelling the effect of cooling rate on tensile properties of 6xxx series aluminium alloys for automotive applications. In *Proceedings of the 2nd conference & exhibition on light materials*. November 8-10, Bremen, Germany.

Myhr, O. R., Grong, Ø., & Andersen, S. J. (2001). Modelling of the age hardening behaviour of Al-Mg-Si alloys. *Acta Materialia, 49*(1), 65–75.

Myhr, O. R., Grong, Ø., & Pedersen, K. O. (2010). A combined precipitation, yield strength, and work hardening model for Al-Mg-Si Alloys. *Metallurgical and Materials Transactions A, 41*(9), 2276–2289.

Myhr, O. R., Grong, Ø., & Schäfer, C. (2015). An extended age-Hardening model for Al-Mg-Si Alloys incorporating the room-Temperature storage and cold deformation process stages. *Metallurgical and Materials Transactions A, 46*(12), 6018–6039.

Pedersen, K. O., Westermann, I., Furu, T., Børvik, T., & Hopperstad, O. S. (2015). Influence of microstructure on work-hardening and ductile fracture of aluminium alloys. *Materials & Design, 70*, 31–44.

Pineau, A., Benzerga, A. A., & Pardoen, T. (2016). Failure of metals I: Brittle and ductile fracture. *Acta Materialia, 107*, 424–483.

Remøe, M. S., Marthinsen, K., Westermann, I., Pedersen, K., Røyset, J., & Marioara, C. (2017). The effect of alloying elements on the ductility of Al-Mg-Si alloys. *Materials Science and Engineering: A, 693*, 60–72.

Ryum, N. (1968). The influence of a precipitate-free zone on the mechanical properties of an Al-Mg-Zn alloy. *Acta Metallurgica, 16*(3), 327–332.

Seyedrezai, H., Grebennikov, D., Mascher, P., & Zurob, H. S. (2009). Study of the early stages of clustering in Al-Mg-Si alloys using the electrical resistivity measurements. *Materials Science and Engineering: A, 525*(1), 186–191.

Shuey, R. T., Tiryakioğlu, M., Bray, G. H., & Staley, J. T. (2006). Toughness after interrupted quench. In *Aluminium alloys 2006 - icaa10*. In *Materials Science Forum: 519* (pp. 1017–1022). Trans Tech Publications.

Stander, N., Roux, W., Basudhar, A., Eggleston, T., Goel, T., & Craig, K. (2015). *Ls-opt user's manual*. Livermore Software Technology Corporation. Livermore, California, USA.

Steglich, D., Wafai, H., & Besson, J. (2010). Interaction between anisotropic plastic deformation and damage evolution in Al 2198 sheet metal. *Engineering Fracture Mechanics, 77*(17), 3501–3518.

Strobel, K., Easton, M. A., Lay, M. D. H., Rometsch, P. A., Zhu, S., Sweet, L., … Hill, A. J. (2019). Quench sensitivity in a dispersoid-Containing Al-Mg-Si Alloy. *Metallurgical and Materials Transactions A, 50*(4), 1957–1969.

Strobel, K., Easton, M. A., Sweet, L., Couper, M. J., & Nie, J.-F. (2011). Relating quench sensitivity to microstructure in 6000 series aluminium alloys. *Materials Transactions, 52*(5), 914–919.

Strobel, K., Lay, M. D. H., Easton, M. A., Sweet, L., Zhu, S., Parson, N. C., & Hill, A. J. (2016). Effects of quench rate and natural ageing on the age hardening behaviour of aluminium alloy AA6060. *Materials Characterization, 111*, 43–52.

Sunde, J. K., Marioara, C. D., van Helvoort, A. T. J., & Holmestad, R. (2018). The evolution of precipitate crystal structures in an Al-Mg-Si(-Cu) alloy studied by a combined Haadf-stem and sped approach. *Materials Characterization, 142*, 458–469.

Toda, H., Oogo, H., Horikawa, K., Uesugi, K., Takeuchi, A., Suzuki, Y., … Kobayashi, M. (2013). The true origin of ductile fracture in aluminum alloys. *Metallurgical and Materials Transactions A, 45*(2), 765–776.

Tvergaard, V. (1981). Influence of voids on shear band instabilities under plane strain conditions. *International Journal of Fracture, 17*(4), 389–407.

Tvergaard, V., & Needleman, A. (1984). Analysis of the cup-cone fracture in a round tensile bar. *Acta Metallurgica, 32*(1), 157–169.

Unwin, P. N. T., Lorimer, G. W., & Nicholson, R. B. (1969). The origin of the grain boundary precipitate free zone. *Acta Metallurgica, 17*(11), 1363–1377.

Vasudévan, A. K., & Doherty, R. D. (1987). Grain boundary ductile fracture in precipitation hardened aluminum alloys. *Acta Metallurgica, 35*(6), 1193–1219.

Werinos, M., Antrekowitsch, H., Ebner, T., Prillhofer, R., Uggowitzer, P. J., & Pogatscher, S. (2016). Hardening of Al-Mg-Si alloys: Effect of trace elements and prolonged natural aging. *Materials & Design, 107*, 257–268.

Westermann, I., Pedersen, K. O., Furu, T., Børvik, T., & Hopperstad, O. S. (2014). Effects of particles and solutes on strength, work-hardening and ductile fracture of aluminium alloys. *Mechanics of Materials, 79*, 58–72.